

Gaia Data Release 3

Microlensing events from all over the sky

Ł. Wyrzykowski^{1,*}, K. Kruszyńska¹, K. A. Rybicki^{1,2}, B. Holl^{3,4}, I. Lecœur-Taïbi⁴, N. Mowlavi^{3,4},
K. Nienartowicz^{4,5}, G. Jevardat de Fombelle⁴, L. Rimoldini⁴, M. Audard^{3,4}, P. Garcia-Lario⁶, P. Gavras⁷,
D. W. Evans⁸, S. T. Hodgkin⁸, and L. Eyer^{3,4}

¹ Astronomical Observatory, University of Warsaw, Al. Ujazdowskie 4, 00-478 Warszawa, Poland

² Department of Particle Physics and Astrophysics, Weizmann Institute of Science, Rehovot 76100, Israel

³ Department of Astronomy, University of Geneva, Chemin Pegasi 51, 1290 Versoix, Switzerland

⁴ Department of Astronomy, University of Geneva, Chemin d'Ecogia 16, 1290 Versoix, Switzerland

⁵ Sednai Sarl, 1204 Geneva, Switzerland

⁶ European Space Astronomy Centre (ESA/ESAC), Villanueva de la Canada, 28692 Madrid, Spain

⁷ RHEA for European Space Agency (ESA), Camino bajo del Castillo, s/n, Urbanizacion Villafranca del Castillo, Villanueva de la Cañada, 28692 Madrid, Spain

⁸ Institute of Astronomy, University of Cambridge, Madingley Road, CB3 0HA, Cambridge, UK

Received 11 April 2022 / Accepted 13 June 2022

ABSTRACT

Context. One of the rarest types of variability is the phenomenon of gravitational microlensing, a transient brightening of a background star due to an intervening lensing object. Microlensing is a powerful tool for studying the invisible or otherwise undetectable populations in the Milky Way, including planets and black holes.

Aims. We describe the first *Gaia* catalogue of candidate microlensing events, give an overview of its content, and discuss its validation.

Methods. The catalogue of *Gaia* microlensing events was composed by analysing the light curves of around 2 billion sources of *Gaia* DR3 from all over the sky covering 34 months, between 2014 and 2017.

Results. We present 363 *Gaia* microlensing events and discuss their properties. Of these, 90 have never been reported before and have not been discovered by other surveys. The contamination of the catalogue is assessed to 0.6%-1.7%.

Key words. Catalogues – Methods: data analysis – Stars: variables: Microlensing

1. Introduction

The gravitational microlensing phenomenon occurs when the light of a background source star is bent by the foreground lens object. Its foundations lie in Einstein's theory of gravity (Einstein 1936), although even Einstein himself was not convinced that the effect could be detectable at all. In part, Einstein was right because such almost-perfect cosmic alignments are extremely rare and the typical angular separations of the images in a single point lens in the Milky Way are of the order of milliarcseconds, and the sources are therefore hard to resolve.

It was only 1986 when Bohdan Paczyński first proposed to look for temporal brightening of stars from the Large Magellanic Cloud (LMC) in order to probe the dark matter halo of the Milky Way for massive astrophysical compact halo objects (MACHOs) (Paczynski 1986). Following this proposal, multiple dedicated large-scale microlensing surveys were launched, namely MACHO (Alcock et al. 1992; Bennett et al. 1993), OGLE (Udalski et al. 1992), EROS (Aubourg et al. 1993), MOA (Abe et al. 1997a; Bond et al. 2001), and KMTNet (Kim et al. 2016), which monitored the Large and Small Magellanic Clouds (LMC and SMC) and also the Galactic bulge and disc. The microlensing era began in earnest with the first microlensing event discoveries (Alcock et al. 1993; Udalski et al. 1993).

The hopes for solving the dark matter problem through microlensing were first raised by the MACHO group (Alcock et al. 1997, 2001a, 2000; Bennett 2005) who claimed there was an excess of microlensing events towards the LMC. If those events could be attributed to compact objects with masses below $1 M_{\odot}$, they would compose up to 20% of the dark matter halo. However, a later study based on the LMC and SMC EROS data (Tisserand et al. 2007) did not see the excess of events and hence placed strong limits on the MACHO content in the halo. Independent verification of this discrepancy came from the OGLE project (Wyrzykowski et al. 2009, 2010, 2011a,b), which concluded that the MACHOs can be almost certainly ruled out for masses all the way up to about $10 M_{\odot}$. This left only a tiny window for dark matter in the form of compact objects in the mass range between 10 and $30 M_{\odot}$, the window recently populated by numerous detections using gravitational wave (GW) signals from merging black holes (Abbott et al. 2021). This, in turn, raised new hopes that at least some of the GWs from black holes are due to dark matter in the form of primordial black holes (Carr 1975; Carr et al. 2016; Bird et al. 2016; García-Bellido & Ruiz Morales 2017).

Microlensing as a tool was also useful in other directions on the sky. The lensing probability increases with the density of sources (Kiraga & Paczynski 1994; Evans & Belokurov 2002) and is the highest towards the Galactic bulge region of the Milky

* e-mail: lw@astrouw.edu.pl

Way. Tens of thousands of microlensing events have been discovered to date by dedicated surveys continuing their operation through recent decades, such as OGLE (Udalski et al. 2015) and MOA (Sako et al. 2008), and initiated recently, namely KMT-Net (Kim et al. 2016). Among those events, as predicted by Mao & Paczynski (1991), signatures for planets accompanying the lensing star were discovered (e.g. Bond et al. 2004; Udalski et al. 2005; Beaulieu et al. 2006; Cassan et al. 2012; Suzuki et al. 2016; Bennett et al. 2021; Poleski et al. 2021) as well as candidates for free-floating planets (e.g. Sumi et al. 2011; Mróz et al. 2017, 2018). Moreover, the large samples of microlensing events allowed the selection of promising candidates for very rare cases of black hole and neutron star lenses (Gould 2000; Mao et al. 2002; Bennett et al. 2002; Wyrzykowski et al. 2016; Wiktorowicz et al. 2019; Wyrzykowski & Mandel 2020; Mróz & Wyrzykowski 2021; Sahu et al. 2022; Lam et al. 2022). Other directions not towards the bulge were also systematically probed by dedicated microlensing surveys (e.g. Derue et al. 2001; Rahal et al. 2009) with the most comprehensive and broad being the recent study by Mróz et al. (2020b).

In the two decades or so, microlensing events have also been serendipitously discovered by large-scale photometric surveys not aiming at microlensing events, such as ASAS-SN (Shappee et al. 2014), ZTF (Bellm et al. 2019), and amateur observers (e.g. Gaudi et al. 2008; Nucita et al. 2018; Fukui et al. 2019). However, it was the *Gaia* space mission (Gaia Collaboration et al. 2016) that was the first to deliver candidate microlensing events from all over the sky at a wide range of magnitudes. *Gaia* Science Alerts (GSA; Hodgkin et al. (2021)), was initiated at the very beginning of the operation of the *Gaia* mission in 2014 to identify ongoing astrophysical temporal phenomena in order to alert the astronomical community and to provide an opportunity to study them in detail. This included a very broad range of events, including supernovae, cataclysmic variables, tidal-disruption events, but also microlensing events. With its first microlensing event discovered in 2016, GSA has so far reported more than 400 candidate microlensing events. This includes spectacular cases such as Gaia16aye (Wyrzykowski et al. 2020), a rotating binary lens event, Gaia18cbf (Kruszyńska et al. 2022), one of the longest microlensing events ever found, and Gaia19bld (Rybicki et al. 2022; Bachelet et al. 2022), a very bright event with the lens mass measured using space parallax, the finite source effect, and optical interferometry (Cassan et al. 2022).

Gaia has been collecting photometric, astrometric, and spectroscopic measurements of nearly 2 billion objects from all over the sky since 2014. The study and classification of objects with photometric time-series until 2017 is one of the main results of *Gaia* DR3 (Gaia Collaboration 2022). In this work, we report the findings of a systematic search for microlensing events in the form of brightening episodes in the photometric time-series data from *Gaia* from years 2014–2017. We perform a statistical study of the collection, present its main properties and potential application for Galactic studies, and report findings from our investigations of individual lensing objects. The uniqueness of the *Gaia* microlensing catalogue is twofold. Firstly, for the first time, the entire sky has been homogeneously monitored for microlensing events. Secondly, *Gaia* has collected time-series of simultaneous three-band photometry for the events as well as astrometric and spectroscopic measurements, which will become fully available in the next *Gaia* data releases, leading to full solutions for the microlensing events reported here.

The paper is organised as follows. In Section 2 we introduce the microlensing models, and in Section 3 we describe the *Gaia*

data and its pre-processing. Section 4 presents the methods used in order to build the catalogue. An overview of the results and the properties of the catalogue are presented in Section 5, while the validation of the sample and a discussion on individual cases are presented in Section 6.

The time-series data used in the paper as well as the parameters of the events are available in the online *Gaia* archive at <http://gea.esac.esa.int/archive/> which contains the table `vari_microlensing` with its fields described in Appendix A. The detailed *Gaia* DR3 documentation and catalogue data model are available at <http://gea.esac.esa.int/archive/documentation/>.

2. Microlensing models

In microlensing, a compact massive object distorts the space-time, forcing the light rays of a background source to change trajectory. In the case of a single point lens, this results in the appearance of two magnified images of the source (Paczynski 1996), typically separated by less than 1 milliarcsecond (Dong et al. 2019). Each lensing configuration, that is, the distance to the lens (or lens parallax, π_L), the distance to the background source (or source parallax, π_S), and the lensing mass (M_L), defines an Einstein ring, with its angular radius:

$$\theta_E = \sqrt{\frac{4GM_L}{c^2}(\pi_L - \pi_S)}. \quad (1)$$

Because of the relative proper motion of the observer, the lens, and the source (μ_{rel}), the source only becomes lensed temporarily when crossing the Einstein ring. As in most cases the two images are not resolvable, the total observed amplification (A) of the source light is the sum of the light of both images (Paczynski 1996) and is described only by one parameter, the projected separation between the source and the lens in units of the Einstein radius as a function of time ($u(t)$):

$$A(t) = \frac{u(t)^2 + 2}{u(t) \sqrt{u(t)^2 + 4}}. \quad (2)$$

In the case of the simplest linear motion of the lens with respect to the source, the separation can be computed as

$$u(t) = \sqrt{\tau(t)^2 + \beta(t)^2}, \quad \tau(t) = \frac{t - t_{\text{max}}}{t_E}, \quad \beta(t) = u_0, \quad (3)$$

where u_0 is the minimal lens–source separation (impact parameter) at the moment of time t_{max} . The duration of the event, which is often referred to as the timescale of the event, or the Einstein time, t_E , depends on the size of the Einstein radius and the relative proper motion, $t_E = \theta_E/\mu_{\text{rel}}$. The bell-like shape of the photometric amplification curve resulting from Equation 2, is now often referred to as the ‘Paczynski curve’.

A standard photometric microlensing event is therefore defined as a temporal increase in brightness of a background point-like object or star. In practice, the total observed brightness of the source is a combination of the light of a background source of flux F_S amplified A -times and possible additional light F_B from unresolved sources within the resolution of the instrument, which might include or be the light of the lens:

$$\text{mag}(t) = \text{mag}_0 - 2.5 \log_{10}(A(t) \times F_S + F_B) = \text{mag}_0 - 2.5 \log_{10}(f_S \times (A(t) - 1) + 1), \quad (4)$$

where we introduce a blending parameter, $f_S = \frac{F_S}{F_S + F_B}$, which defines a fraction of the light of the source in the total observed

flux, that is, $f_s = 1$ for a non-blended source and a dark lens. The mag_0 parameter is the observed brightness of the source and all the blends and is called the baseline magnitude. As the microlensing effect is achromatic, the amplification does not depend on the wavelength. However, only source light is amplified and the spectral energy distribution (SED) of the blend(s) can, in general, be different from that of the source; therefore, any modelling of multi-band data requires independent set of mag_0 and f_s parameters.

In the case of events with timescales of longer than about 20 days, the annual motion of the observer around the Sun can play a significant role and may distort the linearity of the projected lens–source motion (Gould 2000) in a measurable way. In order to account for this effect, which is called microlensing parallax, equation 3 should be modified with the following:

$$\tau(t) = \frac{t - t_{\max}}{t_E} + \delta t, \quad \beta(t) = u_0 + \delta\beta, \quad (5)$$

where

$$(\delta\tau, \delta\beta) = \pi_E \mathbf{\Delta s} = (\pi_E \cdot \mathbf{\Delta s}, \pi_E \times \mathbf{\Delta s}) \quad (6)$$

is the displacement vector due to parallax and $\mathbf{\Delta s}$ is the positional offset of the Sun in the geocentric frame (Gould 2004). The microlensing model with annual parallax has to include a new parameter, the microlensing parallax vector, connected with the parallaxes of the lens, the source, and the Einstein radius, $\pi_E = (\pi_L - \pi_S)/\theta_E$, decomposed into east and north directions, π_{EE} and π_{EN} , respectively.

The microlensing parallax is one of the crucial components needed for determination of the mass and the distance of the lens:

$$M = \frac{\theta_E}{\kappa\pi_E}, \quad \kappa = \frac{4G}{c^2\text{au}} \approx 8.144 \frac{\text{mas}}{M_\odot}, \quad (7)$$

$$\pi_L = \theta_E\pi_E + \pi_S. \quad (8)$$

3. Data

The results in *Gaia* DR3 are based on the first 34 months of *Gaia* observations collected between 25 July 2014 (JD=2456863.9375) and 28 May 2017 (JD=2457901.86389), and spanning a period of 1038 days. On average, in that period each star was scanned by *Gaia* about 40 times. However, this number strongly depends on the region of the sky following *Gaia*'s scanning law (Gaia Collaboration et al. 2016). In particular, the bulge region, where most of microlensing events are expected, was observed typically only about 20 times. Moreover, the data points were not evenly distributed, with pairs separated by 106 minutes because observations were conducted using two of *Gaia*'s telescopes. There were also parts of the sky with an increased number of observations, located near the ecliptic latitudes of $\pm 45^\circ$, where the number of individual epochs per star often exceeded 100.

In this work, we study the photometric G , G_{BP} , and G_{RP} time series in magnitudes and in Barycentric-corrected Julian days, the processing of which is described in detail in Riello et al. (2021) and Eyer et al. (2022). The Microlensing Specific Object Studies (MSOS) pipeline was run together with other variability studies on all *Gaia* DR3 sources. The photometric data were pre-filtered for outliers, as described in Eyer et al. (2022), and only sources with at least ten observations (transits) in G -band were

investigated further. The G_{BP} and G_{RP} band time series were investigated together with the G -band only if there were at least 30 data points available in each band.

As our selection criteria relied on the goodness of the microlensing model fit and the light curves of microlensing events often change over a wide magnitude range, we rescaled the photometric error bars provided with each *Gaia* data point in order to more closely reflect the expected scatter at each magnitude (e.g. Wyrzykowski et al. 2009; Skowron et al. 2016). We used *Gaia* EDR3 mean G versus its standard deviation to derive the expected lowest possible error for each G measurement with its error bar of σ_G^{old} , assuming 30 observations on average per object, using the following formulae:

$$\sigma_G^{exp} = \begin{cases} \sqrt{30} \times 10^{0.17-13.5-5.1}, & \text{for } G < 13.5 \text{ mag} \\ \sqrt{30} \times 10^{0.17G-5.1}, & \text{for } G \geq 13.5 \text{ mag} \end{cases} \quad (9)$$

$$\sigma_G^{new} = \sqrt{(\sigma_G^{old})^2 + (\sigma_G^{exp})^2}. \quad (10)$$

Despite our best efforts to identify and mask the data points outlying significantly from the overall trend of the G_{BP} and G_{RP} light curve, some still remain in the data. In order to avoid the microlensing model being incorrectly driven by those outliers, we rescaled error bars in G_{BP} and G_{RP} time series by a constant factor of 10. This allowed us to continue using the G_{BP} and G_{RP} data points in the microlensing model and minimised the impact of the outliers.

4. Methods

The microlensing events in *Gaia* DR3 were selected among 1 840 947 142 light curves processed by the *Gaia* DPAC Variability Processing Unit CU7 (Eyer et al. 2022). There were two samples created, Sample A based on an automated procedure and selection criteria tuned to *Gaia* light curves (163 events), and Sample B, comprising an additional 233 events selected from the literature, with 33 overlapping with Sample A. The summary of all events, together with the coordinates in equatorial and Galactic frames, the baseline magnitude, and the sample name are presented in Table D.1 of Appendix D. Each *Gaia* source has a unique source identifier (sourceid), but we also introduce here alias names for the *Gaia* DR3 microlensing events in the format GaiaDR3-ULENS-NNN, where NNN is the order number obtained after sorting our catalogue by event baseline magnitudes. Hereafter, we also refer to the events using their numbers (e.g. #001).

The parameters of all 363 events are contained in the *Gaia* DR3 `vari_microlensing` table, and these are listed and described in Table A.1 of Appendix A.

4.1. Sample A

The selection of rare variability types such as microlensing events (typically less than 1 in a million stars, Paczynski 1996) requires a very efficient approach, optimised to work on a large volume of data to be analysed. This was already an issue when the first microlensing searches were conducted on millions of stars in the 1990s (e.g. Alcock et al. 1996; Afonso et al. 2003; Udalski et al. 1994a), as well as in later times, when the number and length of light curves grew significantly in surveys like OGLE, MOA, and ZTF (e.g. Wozniak 2000; Wyrzykowski et al.

2009, 2011a; Sumi et al. 2013; Wyrzykowski et al. 2015, 2016; Navarro et al. 2020b,a; Mróz et al. 2019, 2020b,a; Rodriguez et al. 2021). The common approach among those studies was to first identify all potentially variable stars exhibiting a single episode of brightening, and then study the narrowed-down sample in more detail with more computationally expensive tests. Here, we also followed this philosophy. The main filtering process was divided into two parts, the first called Extractor, and the second being the Microlensing Specific Object Studies (MSOS). Details of the procedure are described in *Gaia* DR3 Documentation, and below we provide a brief outline.

The Extractor studied G , G_{BP} , and G_{RP} data points as well as statistical parameters derived from these time series. It conducted a series of simple and quick tests, in particular, testing whether or not there is a significant number of points brighter than the median magnitude; testing whether or not there is a brightening episode present in all three pass-bands; checking for a unique rise and fall; and checking whether or not the light curve outside of the episode can be considered constant. The Extractor is described in more detail in *Gaia* DR3 Documentation.

Before the next stage, MSOS, there were 98 750 637 sources left for further investigation, which is less than 10% of the original input list. The second part of the pipeline performed a microlensing model fit to the data with the re-scaled error bars, as described in Section 3. The modelling was divided into sub-stages, dubbed ‘Levels’.

Level 0 was the simplest Paczynski model without blending and no annual parallax effect included (Equation 3 and Equation 4 with $f_S \equiv 1$). This model is a good approximation for many microlensing events, especially in less crowded regions of the sky and for faint or dark lenses. This model is also the most mathematically stable. It contains three parameters common for each band (`paczynski0_u0`, `paczynski0_te`, `paczynski0_tmax`), and one additional parameter per band (`paczynski0_g0`, `paczynski0_bp0`, `paczynski0_rp0`).

Level 1 was the standard microlensing model (i.e. with linear relative motion, using Equation 3) which included blending parameters for G -band, G_{BP} , and G_{RP} if enough data points were available in those bands (Equation 4 and f_S defined for each band). The blended model fitting is less stable, in particular for light curves with poorly sampled wings of the microlensing event. The fitting of microlensing parameters in Level 1 (`paczynski1_u0`, `paczynski1_te`, `paczynski1_tmax`), and baselines in each band (`paczynski1_g0`, `paczynski1_bp0`, `paczynski1_rp0`) was initialised with the values obtained at Level 0. Each band had also additional blending parameters initialised for the fitting at 1 (`paczynski1_fs_g`, `paczynski1_fs_bp`, `paczynski1_fs_rp`).

Level 2 model included annual parallax (Eqs 5 and 6), but excluded blending. Blending and microlensing parallax both cause modifications to the standard microlensing light curve, particularly in the region of the wings of the curve. In the case of sparse *Gaia* light curves, the degeneracy between these two parameters can be severe and can prevent the quick convergence of the minimisation procedure.

This Level 2 model contained the standard microlensing parameters as in Level 0 (`paczynski2_u0`, `paczynski2_te`, `paczynski2_tmax`) and two additional ones describing the parallax vector in north and east directions (`paczynski2_parallax_north`, `paczynski2_parallax_east`), as well as baseline magnitudes for each of the bands (`paczynski2_g0`, `paczynski2_bp0`, `paczynski2_rp0`). The Level 2 model was fit only for sources with Level 0 timescale `paczynski0_te` > 20 days, as the

microlensing parallax is not going to be detectable in shorter events.

Finally, all the parameters derived for the models at all Levels, together with their goodness of fit (χ^2/dof) and other statistical parameters (e.g. skewness of the magnitude distribution, Abbe value (von Neumann 1941), amplitudes, etc.) computed for the light curves during the Variability Processing Eyer et al. (2022), were used to derive the membership score and define a set of filters, which were used to select candidates for microlensing events. Details of the selection criteria are described in the *Gaia* DR3 Documentation and briefly in the Appendix. This automated procedure returned 324 candidate events, which were then visually inspected by three independent experienced microlensers and the final sample was composed of 163 events (Sample A). We note that the Level 2 parameters, along with parameters of the Extractor used in the sample selection, were not included in the `vari_microlensing` table of the *Gaia* DR3 release.

4.2. Sample B

In the time period of *Gaia* DR3 (2014-2017), there were other large-scale surveys in operation designed to detect microlensing events. We identified events primarily from the OGLE-IV survey, published separately for the bulge region (Mróz et al. 2019) and the southern Galactic disc (Mróz et al. 2020b). From the most numerous OGLE-IV sample (6251 events), we selected 1527 events that had reported timescales of longer than 20 days and their maximum was between $JD=2,456,863.9375$ and $JD=2,457,901.86389$, which is in the DR3 data span.

In the *Gaia* DR3 data, we also found two bright microlensing events reported by the ASAS-SN survey (Shappee et al. 2014), namely ASASSN-16oe (Strader et al. 2016; Munari et al. 2016) and ASASSN-V J044558.57+081444.6 (Jayasinghe et al. 2017). There were also seven microlensing events identified by the *Gaia* Science Alerts system (Hodgkin et al. 2021) that occurred during *Gaia* DR3 and were added to this sample: Gaia16aua, Gaia16aye (Wyrzykowski et al. 2020), Gaia16bnn, Gaia17ahl, Gaia17aqu, Gaia17bbi, and Gaia17bej.

The cross-match of the selected events with DR3 within 0.5 arcsec yielded a total of 1074 sources; these have been identified as *Gaia* sources. Their time series in G , G_{BP} , and G_{RP} were then processed through the Extractor and MSOS Pipeline and 404 of them were successfully recovered. However, the cuts and filters used for defining Sample A were not applied for this sample. Instead, a visual inspection of the candidates was conducted and 233 events were selected. We required that the event be clearly visible in the *Gaia* data and contain at least two points within the brightening so that the parameters could be determined robustly. As Sample B was composed independently from Sample A, the samples overlapped in 33 cases. The *Gaia* DR3 catalogue contains the same set of parameters for both samples.

4.3. Cross-match with known events

Sample A of events was obtained in an independent procedure and contained 33 events which also ended up in Sample B. In order to assure we identified all possible cross-matches between *Gaia*-discovered events and previously known events, we performed an additional match on the coordinates between Sample A and all available catalogues of candidate microlensing events. The result of the cross-match is provided in Table E.1 in the Appendix, which gathers all matches between *Gaia*-

combined Samples A and B and other microlensing surveys and catalogues containing microlensing events. This includes OGLE-IV bulge (Mróz et al. 2019) and disc (Mróz et al. 2020b) events, the OGLE-IV Early Warning System webpages (Udalski et al. 2015), KMT-Net (Kim et al. 2016), MOA (Abe et al. 1997b), ASAS-SN (Shappee et al. 2014), and GSA-reported microlensing events (Hodgkin et al. 2021). Of 363 events, a total of 273 were alerted by one or more of the above-mentioned surveys (227 cases matched to OGLE-IV alone), and therefore 90 of the events reported here are completely new.

5. Results

We compiled a catalogue of 363 candidates for microlensing events among nearly 2 billion stars monitored by *Gaia* in the years 2014-2017. Below we describe the properties of the catalogue.

5.1. Events location

As expected, the majority of the events, that is 228 events (63%), are located towards the Galactic bulge, defined hereafter in Galactic coordinates as $|l| < 10^\circ$ (see Figure 1), with the highest concentration of events being found at $|b| < 7^\circ$. This is also where most of the events identified before *Gaia* DR3 (from Sample B) are found. The density of events then roughly follows the density of stars, concentrating on the Galactic plane to within 5 to 15 degrees. The Disc sample, defined hereafter as events with Galactic longitudes $|l| > 10^\circ$, contains 135 events (37%) and is mostly concentrated within $|l| < 50^\circ$.

However, there are also individual events at very high Galactic longitudes, reaching as far as the Galactic anticentre (Figure 2). The events with their Galactic coordinates not following the Galactic plane are located in the regions where the density of stars potentially acting as background sources is very low, and therefore the microlensing rate is also very low. Field microlensing events are not unexpected (Nemiroff 1998; Han 2008) and their rate in a survey like *Gaia* (assuming survey depth of $V \sim 19$ mag) is about 0.001 events per year per degree². The presence of events with Galactic latitudes of about 20° is therefore not surprising.

In Figure 3, we plot the locations of all *Gaia* DR3 events together with 343 candidate microlensing events identified by GSA (Hodgkin et al. 2021) in the years 2016-2021. There were only seven events in common between *Gaia* DR3 and GSA (listed in Sample B description). In Figure 3, we emphasise those of GSA candidates, which are brighter at the baseline than $G = 17$ mag. The red lines mark the $\pm 5^\circ$ from the Galactic plane, while the blue lines roughly mark the extent of the Gould Belt, a great circle on the sky drawn by an over-density of young stars and active star formation regions (Taylor et al. 1987; Bekki 2009). We note that the distribution of microlensing events in the southern hemisphere shows a possible over-density that coincides with the Gould Belt. This could suggest that at least some of the events in those parts of the sky could be due to lenses originating from the enhanced stellar density in the Belt, with sources from the background Galactic disc.

We find no events in or near the Magellanic Clouds. Despite initial claims of an excess of events and their possible origin in low-mass halo, dark-matter compact objects (Alcock et al. 1997, 2000; Bennett 2005), the event rate in that direction has now been established to be very low and consistent with events caused by the lenses from within the Clouds (Sahu 1994; Tisserand et al. 2007; Wyrzykowski et al. 2011b).

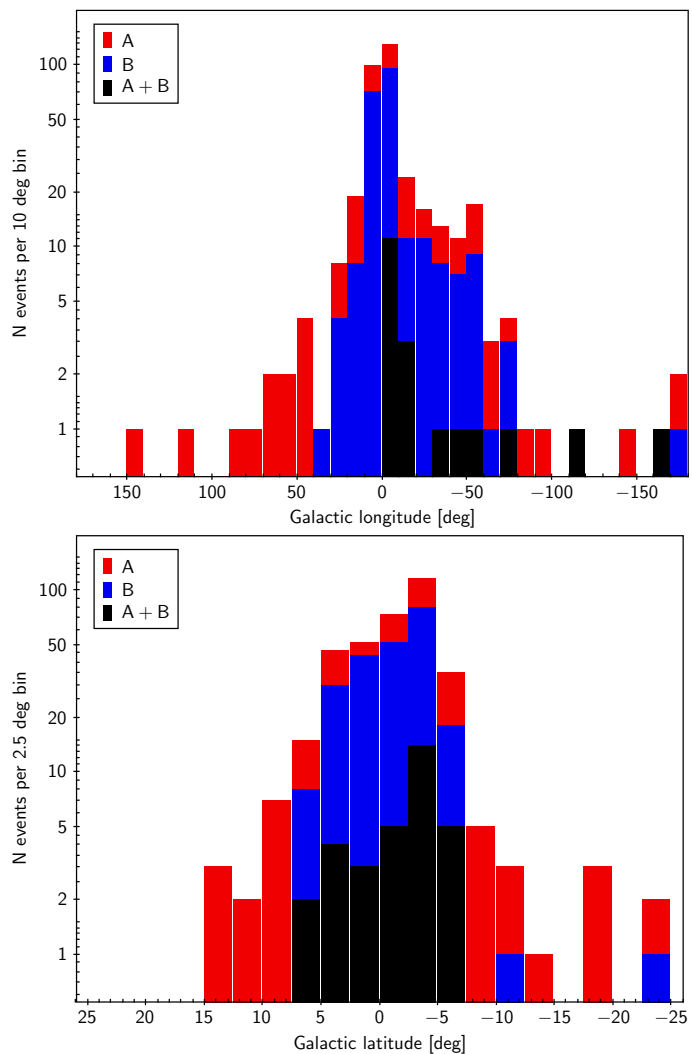


Fig. 1. Distribution of *Gaia* microlensing events over the sky in Galactic longitude (top panel) and latitude (bottom panel). Events from samples A and B and their overlap are marked with different colours.

5.2. Properties of the events

Figure 4 shows the distribution of the times of the maximum (t_{\max}) of events from Sample A, B, and their overlap (A+B) from the Level 0 microlensing model fit. The application of filtering on the moment of the maximum of an event resulted in the cuts seen for Sample A, where events found automatically have been restricted to fall within the *Gaia* DR3 data time-span. This filter was not applied for Sample B (events from the literature with sufficient *Gaia* data to derive their parameters) and there are some events with their maxima outside of the *Gaia* DR3 time-span. All of these are the events with timescales longer than 100 days, and therefore their light curves are still well defined within the *Gaia* DR3 data time window.

The distribution of G baseline magnitudes found in the fitting procedure at Level 0 (paczynski0_g0) is shown in Figure 5. The full sample contains events with a baseline spanning a very wide range of magnitudes, from 13 to 21 mag. However, due to filtering of events fainter than 19 mag in the baseline, the Sample A does not contain fainter events, while the Sample B contains 98 events between 19 and 21 mag in G , with the faintest baseline being 20.97 mag for GaiaDR3-ULENS-363/OGLE-2017-BLG-0116/

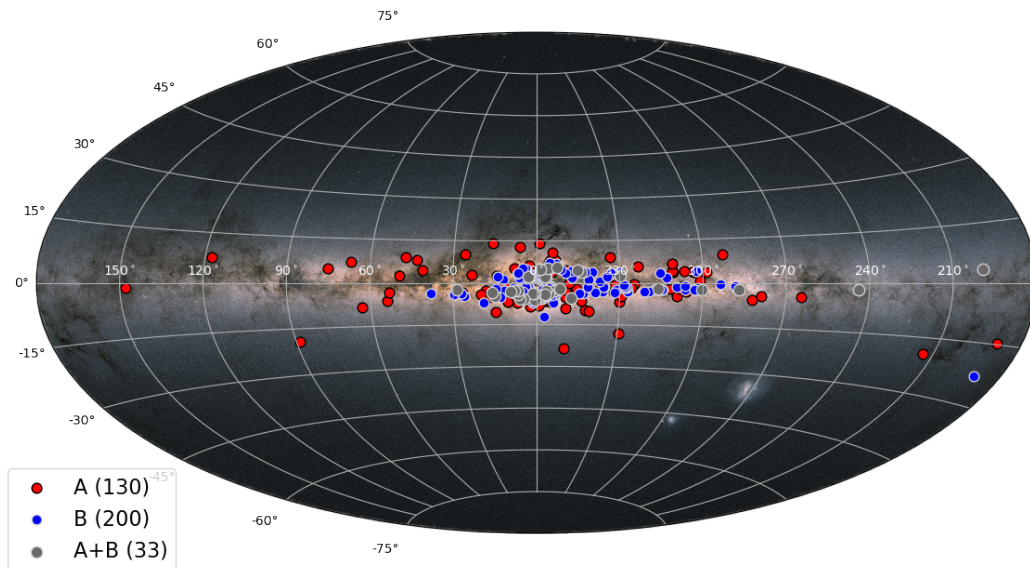


Fig. 2. Distribution of the microlensing events on the sky in Galactic coordinates in degrees over-plotted on the *Gaia* EDR3 sky map.

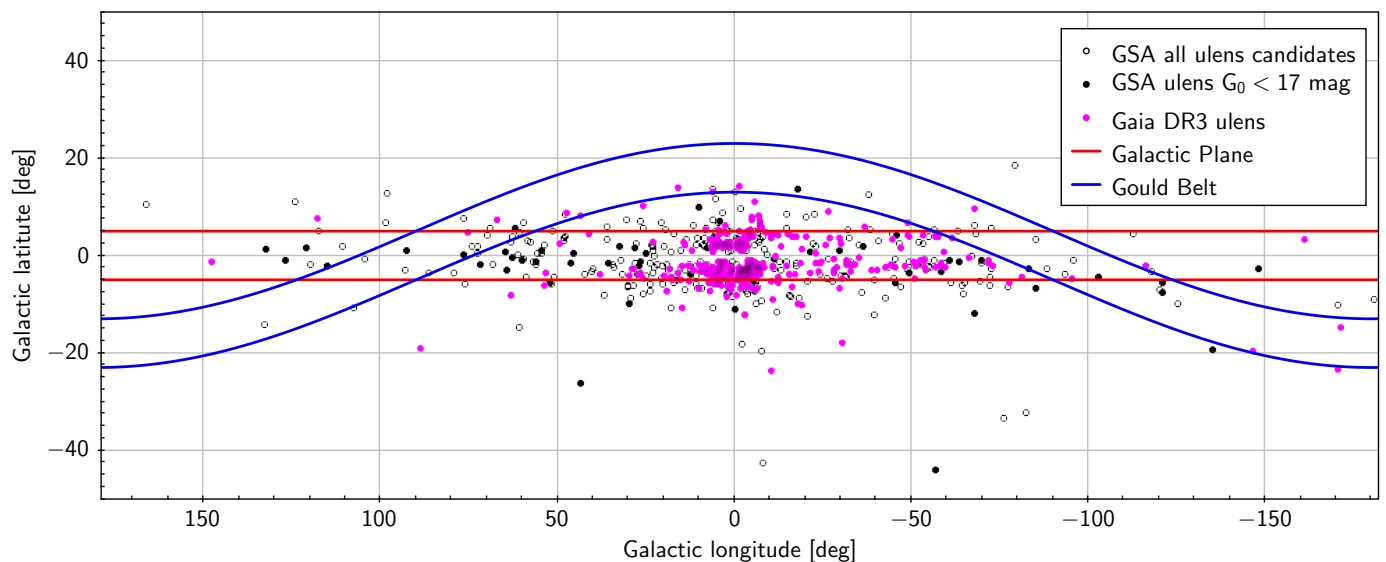


Fig. 3. *Gaia* DR3 microlensing candidates together with 343 candidates for microlensing events identified by GSA in the years 2016-2021. The red belt denotes the Galactic plane, while the blue lines roughly mark the location of the Gould Belt.

KMT-2017-BLG-1029 (sourceid=4067300223660786304). At the other end of the magnitude scale, there is a number of events with very bright baselines, with as many as 65 events brighter than $G = 17$ mag. The brightest in the sample (sourceid = 6059400613544951552) has a baseline of $G = 13.58$ mag and therefore it holds an alias name GaiaDR3-ULENS-001. Such bright events are going to be the most suited for *Gaia* astrometric time-series studies, as shown in Rybicki et al. (2018). Of eight events brighter than $G = 15$ mag, six are new events that have not been seen by any other survey (see Section 4.3).

Figure 6 shows the distribution of Level 0 timescales (paczynski τ_0) for Sample A, Sample B, and the overlap between the samples. The Level 0 timescale, when multiplied by a factor of about 6, is a good indicator of the event duration, that is, the time during which the magnification caused a significant deviation from the baseline. For Sample A, the shortest timescale

is about 20 days and the longest is 250 days; these ranges of timescales are set at the filtering process to generate that sample. Events in Sample B were not restricted by their timescales and there are single and most likely unrealistic cases as short as 1.5 days and as long as 5000 days. However, most events have a timescale of about 50 to 70 days.

5.3. Source and lens distance from *Gaia*

Figure 7 shows the parallaxes measured by *Gaia* EDR3 for sources where microlensing events were identified. We split the A and B samples into sources with reliable and unreliable astrometric measurements. We used the RUWE parameter (Lindgren et al. 2021) as an indicator for sources where the parallax value should not be trusted (other indicators include Astrometric Excess Noise from *Gaia* or astrometric fidelity from Rybizki et al.

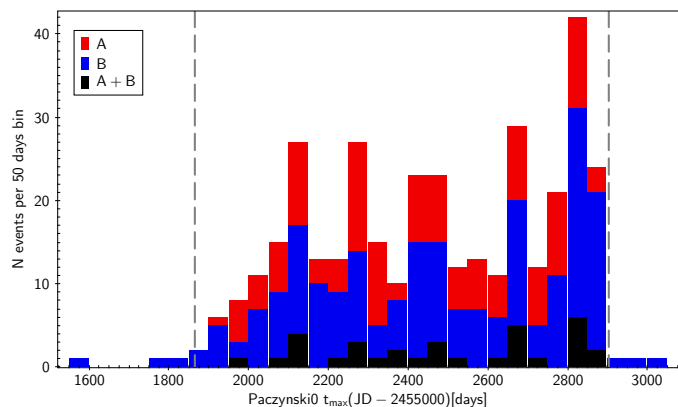


Fig. 4. Distribution of the Level 0 parameter for the time of the maximum (t_{max}) of *Gaia* DR3 microlensing events. The dashed lines indicate the *Gaia* DR3 data time-span.

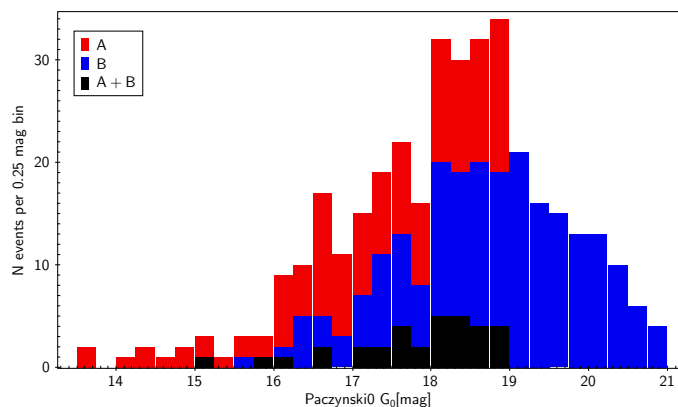


Fig. 5. Distribution of Level 0 G baseline magnitudes of *Gaia* DR3 microlensing events.

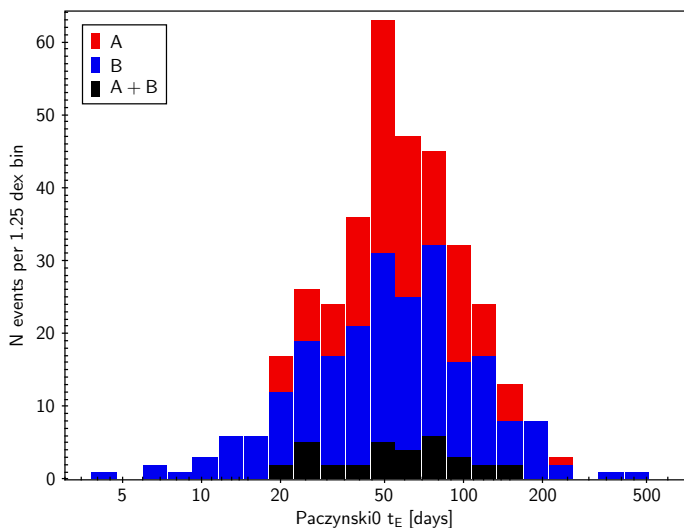


Fig. 6. Distribution of timescales for *Gaia* DR3 microlensing events obtained in the simplest Level 0 microlensing fit.

2022). Most of the non-reliable parallax measurements are located in the densest parts of the Galactic plane, in the bulge. The negative parallaxes are also very common there because most sources are at a relatively large distance and the precision of their parallaxes is insufficient because of crowding and a very

low number of epochs, which in *Gaia* DR3 is typically less than 30.

Among 363 events, there were 346 sources for which a distance was computed by Bailer-Jones et al. (2021) using *Gaia* EDR3 parallaxes. Within that sample, we selected those sources that had $RUWE < 1.5$ and $parallax_over_error > 1$ to guarantee the geometric parallax measurement was robust and the astrometry was not affected by any effects, such as binarity (Belokurov et al. 2020) or astrometric microlensing (Dominik & Sahu 2000; Belokurov & Evans 2002; Rybicki et al. 2018; Klüter et al. 2018).

However, in order to correctly utilise *Gaia* distances in applications to microlensing events, the blending parameter in G -band, $paczynski1_fs_g$, is required. This parameter informs us about the amount of light that is magnified in a microlensing event, with values close to 1 indicating no or very little additional constant light. The extra light might originate from an unassociated star or, most naturally, from the lens itself. In the densest stellar regions of the Galaxy, towards the bulge, the blend is likely to be a random star unrelated to the event and located within the resolution of the instrument. In turn, in the less crowded Galactic plane disc region, it can be quite safely assumed that the blended light comes from the lens.

Relying on the hypothesis that the blending light is the light of the lens, we can use *Gaia* parallaxes to derive some of the parameters of the microlensing events. In a general case, the parallax measured by *Gaia*, π_G , is a linear combination of source parallax, π_S , and lens parallax, π_L : $\pi_G = \pi_S f_S + \pi_L (1 - f_S)$. This is also valid analogously for the proper motions. If the blending parameter is near 1, meaning most of the light seen in the baseline is coming from the lensed source, then the astrometric parallax and proper motion signal are primarily induced by the motion of the source. On the other hand, with the blending parameter value approaching 0, the dominant light is that of the blend (lens). Intermediate values of f_S are mixed cases and *Gaia* parallaxes can be used to derive lens parallax only if the source distance is measured with other means. In the case of microlensing events, the fact that only the source light is amplified during the event can be used in spectroscopic follow-up observations carried out on an ongoing event near its maximum brightness and hence the spectroscopic distance to the source can be estimated (e.g. Bachelet et al. (2022)).

Figure 8 shows distances as derived by Bailer-Jones et al. (2021) based on *Gaia* EDR3 data for events with extreme values of their blending parameter, $paczynski1_fs_g$, as a function of Galactic longitude. Only objects with $RUWE < 1.5$ and $parallax_over_error > 1$ were considered. The sample was divided into 89 source-dominated events ($paczynski1_fs_g > 0.9$) and 14 lens-dominated events ($paczynski1_fs_g < 0.2$). The bulk of sources in events located towards the Galactic bulge are clearly located in the bulge itself at distances of 6–9 kpc. There is also a number of sources at much shorter distances of about 2–4 kpc. In the disc fields, the distances are spread from 1 to 8 kpc. Of particular importance are the three events at large Galactic longitudes (#32, #137 and #153), with source distances estimated to ~ 1 kpc. If the blending parameter in those cases was determined correctly, this suggests that very nearby sources indicate even closer lenses. This would be somewhat surprising for events located in the very low-stellar-density regions of the sky, unless these events can be associated with the over-density of the Gould Belt (Figure 3). Two of these three (#32, 3292310414861319936 at 1300 pc and #137, 3012224323198211968 at 500 pc) are indeed located on the sky within the southern part of the Gould Belt. The northern

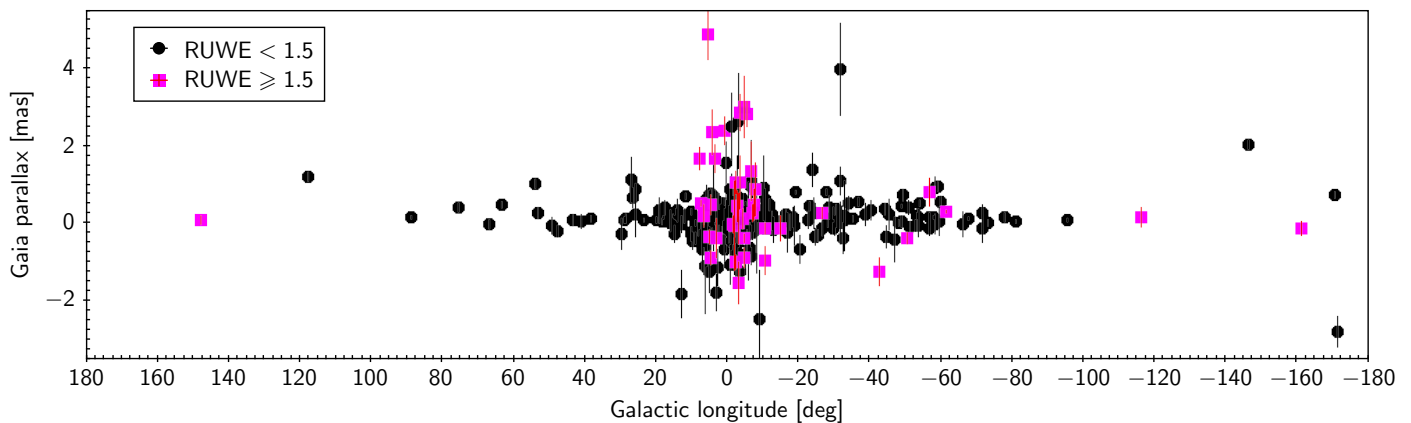


Fig. 7. *Gaia* EDR3 geometric parallaxes for *Gaia* sources with microlensing events, split by the reliability of the parallax using the RUWE parameter. Circles denote $\text{RUWE} < 1.5$, squares denote $\text{RUWE} \geq 1.5$.

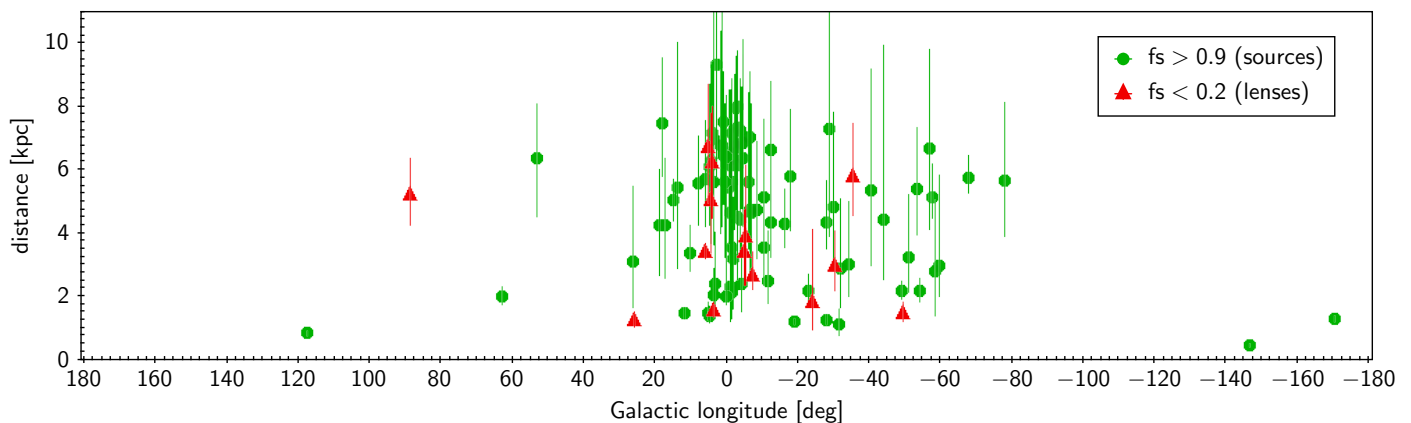


Fig. 8. *Gaia* EDR3 geometric distances from Bailer-Jones et al. (2021) for sources and lenses in *Gaia* events, filtered on $\text{RUWE} < 1.5$ and $\text{parallax_over_error} > 1$ and divided into source-dominated events ($\text{paczynski1_fs_g} > 0.9$, green circles) and lens-dominated events ($\text{paczynski1_fs_g} < 0.2$, red triangles).

event (#153, 2214532279378994816 at 900 pc) is positioned far from both the Gould Belt and fairly far from the Galactic plane ($b \sim 7^\circ$), and therefore seems to be a genuine field event (Han 2008). We note that the light curve of event #137 shows a strong signature of microlensing parallax and a more detailed analysis of this event is necessary to derive both the microlensing parallax and the correct blending parameter. Moreover, event #137 could actually be a young stellar object (YSO; see Section 6.3); in such a case its distance would agree with its association to the Gould Belt.

There are 14 events in which the blending parameter indicated strong domination of the light from the lens in the microlensing curve. In such cases, it is possible that the *Gaia* parallax is the actual measurement of the parallax of the lens and the distance to the lens can be directly obtained. Figure 8 shows their distances from Bailer-Jones et al. (2021) as a function of Galactic longitude. There is a range of lens distances in that sample, from objects at 1-2 kpc to 6 kpc, suggesting that lensing originates from both the Galactic disc and the bulge. We note that, if the microlensing parallax π_E was detected and measured in such microlensing events, and the source distance π_S was known from spectroscopy for example, the size of the Einstein radius, and therefore the mass of the luminous lens (Equation 7), could be determined, as $\theta_E = \frac{\pi_L - \pi_S}{\pi_E}$. The microlensing parallax determination for the events in this sample requires a detailed and dedicated study, which is beyond the scope of this paper.

5.4. Colour–magnitude diagrams

Colours and colour–magnitude diagrams (CMDs) of microlensing events can be useful in studying the populations of sources, lenses, and individual events. In a genuine microlensing event, the colour, in principle, should not change throughout the event, unless there is blending with an object that has a different colour from that of the source. The colour of a *Gaia* microlensing event could be obtained from the G_{BP} and G_{RP} time series, but there were only 155 events for which there are at least 30 data points available in both bands. Moreover, in a couple of cases, the fitting procedure for G_{BP} or G_{RP} time series failed to find the correct values of the baselines (e.g. #284, 4061109904516035840). On the other hand, there were 355 events for which *Gaia* DR3 $G_{BP} - G_{RP}$ colours were derived from integrated G_{BP} and G_{RP} fluxes from the *Gaia* on-board spectrophotometers (Gaia Collaboration et al. 2016), which were computed as means based on the entire *Gaia* DR3 time series. Any chromatic changes in microlensing events would naturally affect the colour, but in most cases it can be assumed as a good proxy of the colour.

The plots in Figure 9 show the observed colour–magnitude diagrams for the bulge ($|l| < 10^\circ$) and disc ($|l| \geq 10^\circ$) regions. The background shows distributions of mean magnitudes and colours of stars in typical fields for each of the regions. Overplotted are the microlensing events for which the $G_{BP} - G_{RP}$ colours were available in *Gaia* DR3 (355 sources). The selection cut for Sample A required the median BP minus median RP

to be between 1 and 4 mag and baseline magnitude brighter than $G = 19$ mag (see Appendix C); therefore, all faint and very red events belong to Sample B. For the bulge region, there are many events located outside of the main locus of stars and their density roughly follows the direction of the interstellar extinction. An additional probable reason for the objects located at red colours is the blending of the source with a much redder lens or blend, or vice versa. For the disc, as expected, the effect of the extinction is not as pronounced as in the bulge and the events roughly follow the two main loci where the disc stars are concentrated.

The colour and the baseline magnitude are affected by blending in a similar way to the *Gaia* parallax, as discussed earlier. This means that the CMD locations of events can only be interpreted correctly in extreme cases of blending parameters. Therefore, for the events with all blending parameters (`paczynski1_fs_g`, `paczynski1_fs_bp`, `paczynski1_fs_rp`) larger than about 0.9 it can be assumed that their observed quantities are related to the microlensed source star. In the opposite case, where blending is smaller than about 0.2, the magnitudes and colours would refer to the blend and possibly to the lens itself.

We computed the absolute magnitudes and colours of the sources and lenses that are only defined by the `paczynski1_fs_g` parameter, which also has well-defined parallaxes from *Gaia*, requiring $\text{RUWE} < 1.5$ and $\text{parallax_over_error} > 1$. Figure 10 shows the absolute magnitude for a selection of stars from typical bulge and disc fields, requiring $\text{parallax_over_error} > 1$ with over-plotted microlensing events and their sources and lenses, depending on the blending parameter. In the bulge region, there are sources that can be clearly associated with the bulge stars; this includes both red clumps and main sequence stars. There are also redder sources, of which the vast majority are probably the red clump giants affected by the high level of interstellar extinction. In the disc, the majority of sources are associated with the main sequence stars, with only one or two sources belonging to the red clump giant population. As for the luminous lens candidates, in the bulge region there are cases of main sequence stars, red clump stars, and possibly a reddened red clump lens. For the disc, there are both main sequence star lenses and one possibly due to a red clump star.

5.5. Timescale distributions

The Einstein time (tE), or event timescale, is the only parameter of the standard Paczyński microlensing model that carries information about the physical parameters of the event (see Section 1). For an individual event, the measurement of its timescale is only an indication of the size of the Einstein radius (θ_E) and the relative proper motion (μ_{rel}). When combined with the measurement of the microlensing parallax, it can already be used to guess the mass of the lens by employing expected and typical values for the proper motion; see for example Bennett (2005); Skowron et al. (2011); Batista et al. (2011); Wyrzykowski et al. (2016). However, in the case of an individual event, the complete solution of the event, that is, computation of the lens mass and its distance, can only be achieved if the angular Einstein radius θ_E is measured indirectly; for example through a finite source effect in single (Zub et al. 2011; Yoo et al. 2004) or binary lenses (Alcock et al. 2001b; An et al. 2002), or directly using high-angular-resolution imaging and interferometry (e.g. Kozłowski et al. 2007; Dong et al. 2019; Cassan et al. 2022) or astrometric microlensing (e.g. Sahu et al. 2014, 2017; Kains et al. 2017; Rybicki et al. 2018; Sahu et al. 2022; Lam et al. 2022).

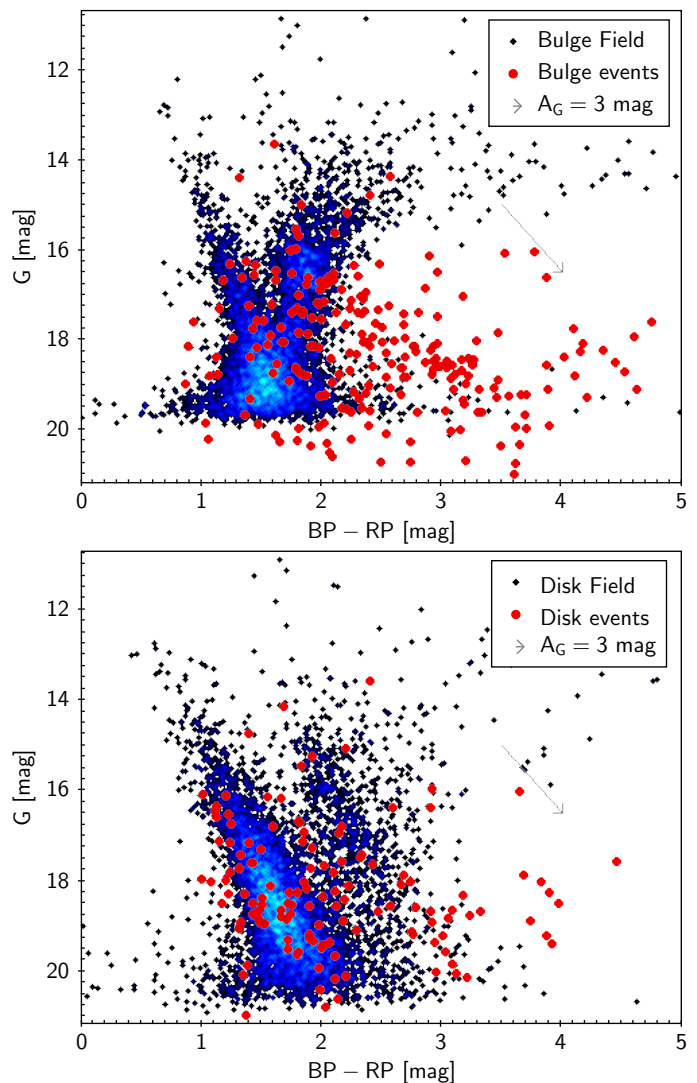


Fig. 9. Colour–magnitude diagrams as observed by *Gaia* (black/blue points) for a typical bulge field (upper panel) and typical disc field (lower panel). The positions of microlensing events are displayed based on their average $G_{\text{BP}} - G_{\text{RP}}$ colour from *Gaia* DR3 and their baseline G magnitude from Level 0 fit.

If the timescales are derived for a larger sample of events, they can be used to study the properties of the population of the lens. As shown already in Kiraga & Paczynski (1994), the total optical depth for microlensing, which is measured from a distribution of event timescales, depends on the total mass of the lenses. The subsequent catalogues of microlensing events towards the Galactic bulge (e.g. Udalski et al. 1994b; Afonso et al. 2003; Popowski et al. 2001; Sumi et al. 2013; Wyrzykowski et al. 2015; Mróz et al. 2019) as well as in the direction of the Galactic disc (e.g. Rahal et al. 2009; Mróz et al. 2020a,b; Rodriguez et al. 2021) can help us to compare the Galaxy models with the observations (e.g. Evans & Belokurov 2002; Wegg et al. 2016).

The *Gaia* microlensing events reported here form a fairly small sample compared to the thousands of events reported by other longer and more sensitive surveys. In Sample A, which was produced by an automated procedure and human vetting, the measured timescales span from 20 days up to about 300 days if no blending is modelled, and up to 2000 days if the blending is included. This is clearly a tail of the bulk of the distribution, as in the direction of the central part of the bulge the mean timescale

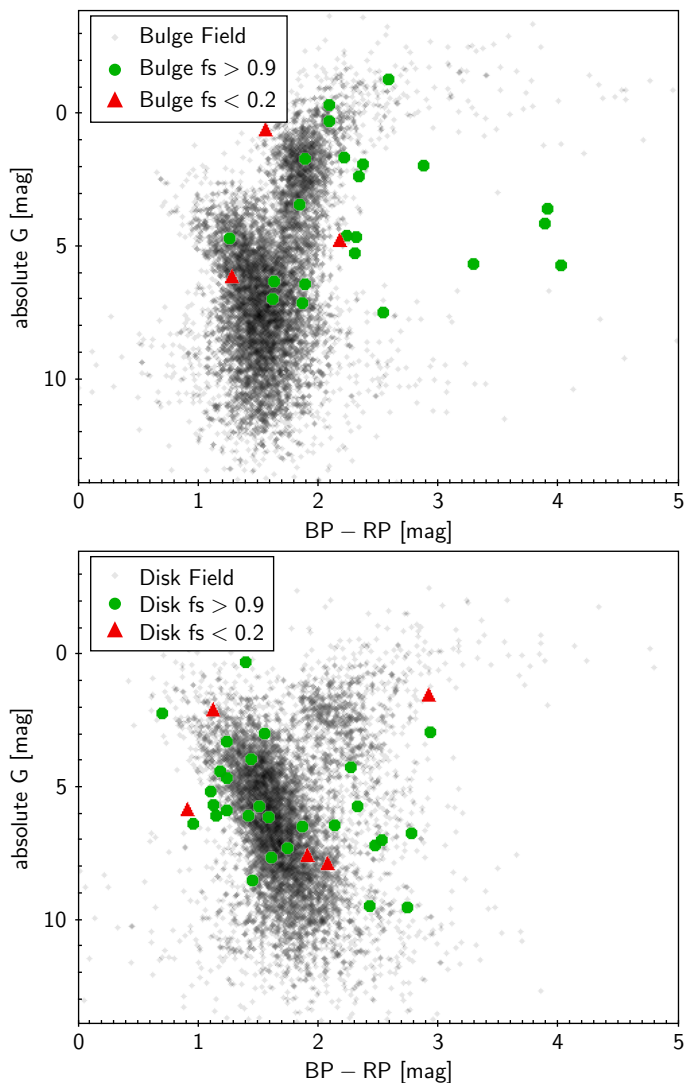


Fig. 10. Colour–magnitude diagrams with absolute G derived using *Gaia* EDR3 parallaxes. The same typical stellar field was used for bulge (upper plot) and disc (lower plot) as in Figure 9 (black/blue points), with the cut on *parallax_over_error* > 1 . The baseline magnitudes from Level 1 were used to show microlensing events for G -band as well as for the colour computation. Baseline magnitudes most likely indicate the source for non-blended events ($f_s > 0.9$) and the lens for highly blended events ($f_s < 0.2$).

is about 28 days (Wood & Mao 2005; Wyrzykowski et al. 2015; Mróz et al. 2019). As noted in Mróz et al. (2019), the timescales of events tend to increase with increasing Galactic longitude, with 22 days near $l \sim 0^\circ$ to 32 days at $l \sim 8^\circ$. The increase in timescale is due to the fact that in the directions far from the bulge, both lenses and sources are located in the disc and often have similar transverse velocities. Moreover, the increase in timescale is not symmetric around $l = 0$, as it reflects the presence of the inclined Milky Way bar, causing longer timescales at negative longitudes (Stanek et al. 1994; Kerins et al. 2009; Wyrzykowski et al. 2015; Wegg et al. 2016; Awiphan et al. 2016; Mróz et al. 2019).

We tried to see those trends in the mean timescales of *Gaia* events. Figure 11 shows the timescales of all events on a map in Galactic coordinates. We used a smaller sample of events that overlapped with those of OGLE in order to derive a rough corrected timescale distribution. Mróz et al. (2019) and Mróz et al.

(2020b) computed the detection efficiency curves as a function of t_E for their OGLE-IV bulge and disk samples, respectively. This function shows the change in the sensitivity of the survey to events at different timescales. Only efficiency-corrected timescale distributions are suitable for comparison with the Galaxy model predictions, as survey-specific effects, such as cadence, survey duration, and seasonal and weather gaps, can limit the sensitivity to different timescales. For the *Gaia* events sample it would not be trivial to derive such a function, as this would require a full and detailed simulation of the spacecraft observations and the events detection pipeline. Moreover, part of our pipeline still involved humans, and therefore such a process would be hard to reproduce.

Nevertheless, in order to estimate the mean timescale distribution for the all-sky sample of events found in *Gaia*, we compared the efficiency-corrected timescale distributions of OGLE events with our events in the bulge ($|l| < 10^\circ$) and in disc separately. We applied a magnitude cut at $G_0 < 19$ mag to guarantee that we compare similar populations of sources and we find a rough ratio between mean timescales of 2.5 and 2, for bulge and disc, respectively. We computed the mean timescale for the blended model (Level 1) for events from Sample A by modelling their distributions in log-space with a Gaussian. We divided the sample into three major sky sections: inner bulge ($|l| < 5^\circ$), outer bulge ($5^\circ < |l| < 10^\circ$), and the remaining events as disc ($|l| > 10^\circ$). The distributions and their Gaussian fits are shown in Figure 12. We find means of 56, 79, and 72 days, for the inner bulge, outer bulge, and disc, respectively. Applying the correction derived from the comparison of *Gaia* and OGLE-IV samples (2.5 for bulge fields and 2 for disc), we obtain mean timescales varying from 22 to 32 days between inner and outer bulge and about 36 days for the disc events. This is in a close agreement with the findings for much larger samples of events found by OGLE (Wyrzykowski et al. 2015; Mróz et al. 2019, 2020b) and MOA (Sumi et al. 2013) surveys. We note that our sample is far too small to attempt whole-sky mean timescale computations.

6. Discussion

The *Gaia* DR3 catalogue of microlensing events contains 363 unique sources spanning a wide range of baseline magnitudes, amplitudes, and timescales. The validation of the catalogue can be assessed most efficiently by comparing the *Gaia* detections with those from the OGLE-IV survey (Udalski et al. 2015), which operated and observed both the bulge and southern Galactic plane within the time-span of the DR3 data collection (2014–2017). In the direction of the bulge, OGLE-IV conducted a monitoring of stars to about $I < 21$ mag with varying cadence, spanning from tens of observations per night for the densest parts of the bulge (± 5 degrees in Galactic longitude and latitude around the Galactic centre) to observations separated by a couple of nights in the regions of the bulge with the lowest stellar density. More details on the OGLE-IV observing strategy can be found on the OGLE webpages¹ and in Udalski et al. (2015). The Galactic plane has been observed by the OGLE-IV survey since 2013 with much sparser cadence spanning from a couple of days to weeks and with the depth of about $I < 20$ mag, but covering the entire southern Galactic plane to about $\pm 7^\circ$ in Galactic latitude. More details on the Galactic plane survey can be found in Mróz et al. (2020b).

¹ <https://ogle.astrouw.edu.pl/>

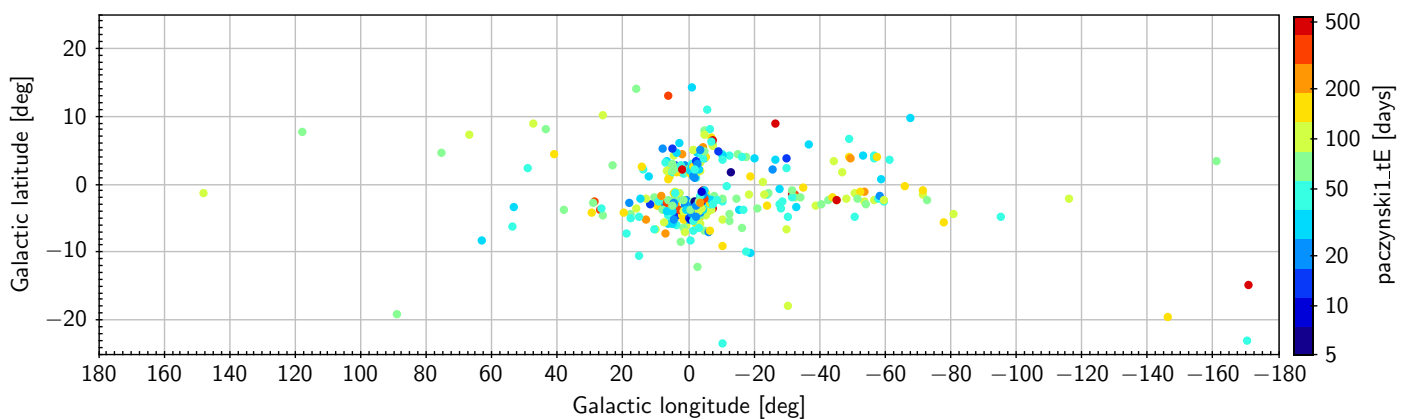


Fig. 11. Map of *Gaia* microlensing events in Galactic coordinates, with colour encoding their Level 1 timescale.

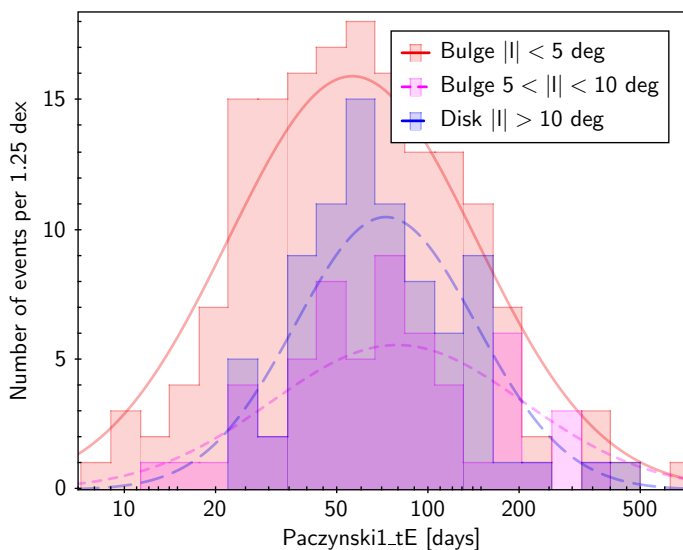


Fig. 12. Distributions of Sample A microlensing events in different Galactic longitude bins together with the Gaussian model fits.

6.1. Completeness

We use OGLE-IV bulge and disk samples to assess the completeness of the *Gaia* microlensing events catalogue. In total, there were 227 events from Samples A and B that overlapped with the OGLE-IV catalogues, with 33 events found independently in *Gaia* data (Sample A and A+B) and 194 events solely in Sample B. Figure 13 shows the timescales and baseline magnitudes of bulge ($|l| < 10^\circ$) and disc ($|l| \geq 10^\circ$) events. *Gaia* events clearly coincide with the brighter and longer section of the diagram. The OGLE bulge events are dominated by baselines fainter than $G = 20$ mag and their typical timescales are about 30 days. In *Gaia*, the bulk of the events is bright, which is a result of one of the cuts on Sample A ($G < 19$ mag). All events fainter than $G = 19$ mag are from Sample B. In the disc, the OGLE and *Gaia* samples overlap more closely than in the case of the bulge, but still the difference in the baseline magnitude coverage is different, with OGLE reaching fainter baselines.

We calculated the completeness in magnitude space by comparing bulge and disc samples of *Gaia* events with the OGLE-IV events, limiting the latter sample to events found during the time-span of *Gaia* DR3 data collection. Figure 14 shows completeness as a function of baseline magnitude in G . For the bulge events, the function peaks at about 17 mag at about 30%, drop-

ping to a couple of percent at the faintest end. For the disc, the completeness is significantly better as it reaches nearly 80% at 17 mag and has another peak at about 19 mag at $\sim 70\%$. The poor performance of *Gaia* itself in the bulge region due to high stellar density (Fabricius et al. 2021). Additionally, the bulge is one of the least frequently scanned parts of the sky (typically about 30 epochs within *Gaia* DR3), and therefore the detection efficiency of microlensing events is low there. In contrast, Galactic disc regions of the sky receive up to the maximum cadence possible with *Gaia*, with the numbers of epochs varying from about 70 to 140 in DR3. There is also a possibility that the OGLE-IV survey is not fully complete in the disc regions, as their cadence is sparser and the depth is shallower than in the bulge. In such a case, *Gaia* completeness would actually be lower than that measured above.

The completeness of the event timescales can also be derived by comparing with the OGLE bulge and disk samples. In order to ensure a fair comparison, we limited OGLE events from Mróz et al. (2019) and Mróz et al. (2020b) to those with their maxima within the *Gaia* DR3 time-span and we cut OGLE and *Gaia* samples on a baseline magnitude of $G = 19$ mag. Figure 15 shows the histograms of such trimmed OGLE and *Gaia* samples, again for the bulge and disc events. In the bulge, the completeness varies from 0% for events with timescales shorter than 7 days to about 50% for events with timescales of about 60 days and approximately 30% for events with timescales of 100 days. For the disc, the numbers of events from both *Gaia* and OGLE-IV are fairly small, but the completeness is significantly higher than in the bulge. At about 30 days and 140 days, nearly 100% of events were recovered by *Gaia*, while for the shortest timescales, recovery was only about 20%. The main reason for this very low recovery rate of short events is again *Gaia*'s scanning law, which generates a scanning pattern in which *Gaia* observes the same spot on the sky typically after about 30 days. The detection efficiency drops for the longest timescales in both bulge and disc cases because of the limited time-span of the *Gaia* DR3 data (about 1000 days).

6.2. Parameter accuracy

The most important parameter of a standard, non-parallax single-point-source, single-point-lens microlensing event is its timescale, t_E , as this contains information about the physical properties of the lens. Figure 16 compares the values of the Einstein timescale as derived by *Gaia* and OGLE for the

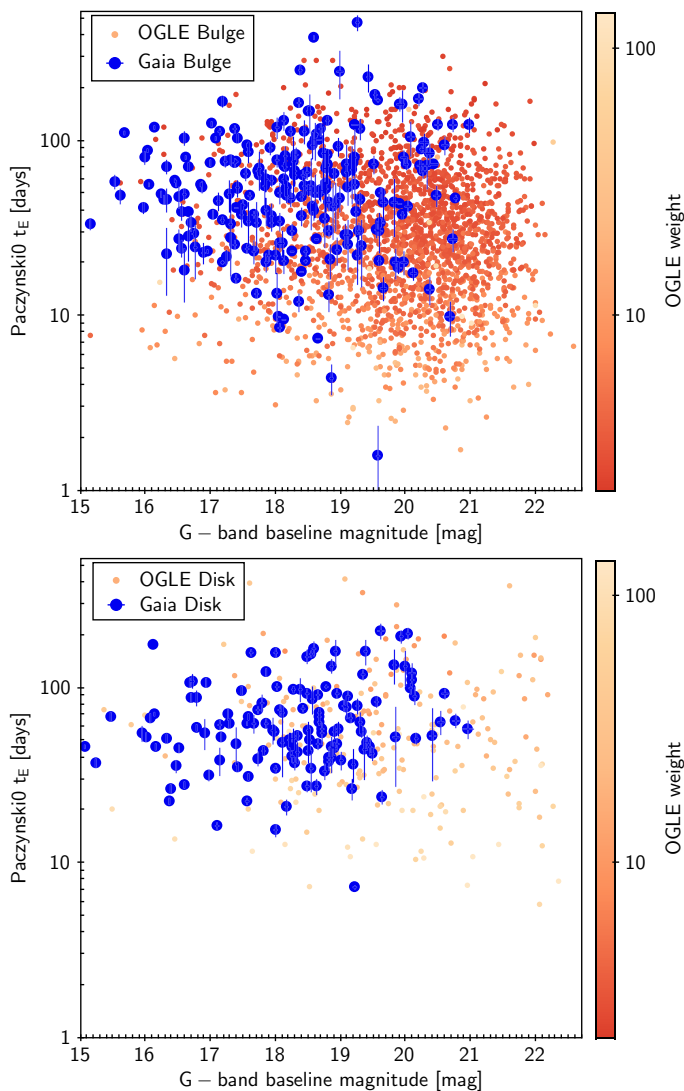


Fig. 13. Comparison of *Gaia* event timescales and baseline magnitudes with OGLE-IV events for the bulge (top) and disc (bottom) samples. Colour shading for OGLE points indicates the weight, which reflects the detection efficiency of the OGLE survey (Mróz et al. 2019, 2020b). Only OGLE events that occurred during the DR3 time range are shown.

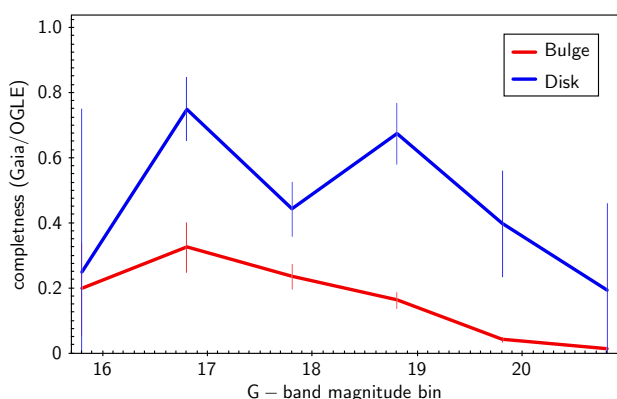


Fig. 14. Completeness of the *Gaia* DR3 microlensing events sample as a function of *G*-band baseline magnitude. Completeness was derived by identifying matches of *Gaia* and OGLE-IV event catalogues and was derived separately for the bulge and disc sections.

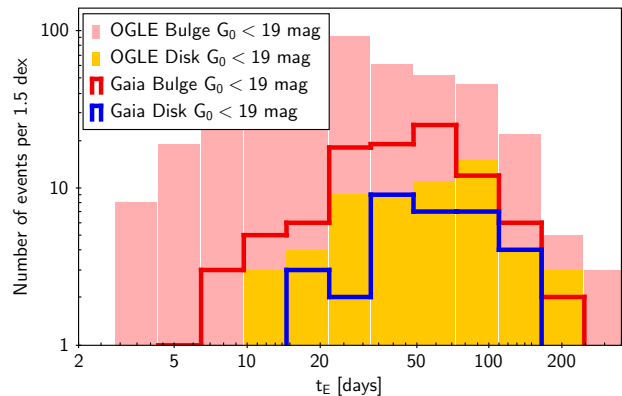


Fig. 15. Comparison of the distributions of event timescales for *Gaia* DR3 microlensing events found also by the OGLE-IV in the bulge and disc regions, cut at the baseline magnitude of *G* of 19 mag. Parameter `paczynski0_te` was used for *Gaia* events and $t_{E(\text{best})}$ for OGLE-IV events.

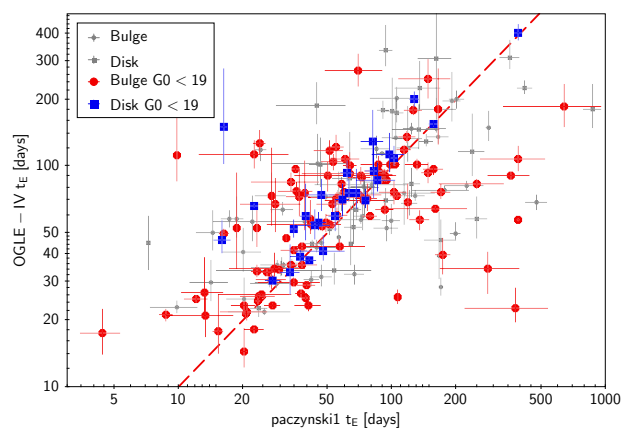


Fig. 16. Comparison of timescales derived for *Gaia* DR3 microlensing events also found by the OGLE-IV for bulge and disc. Parameter `paczynski1_te` was used for *Gaia* events and $t_{E(\text{med})}$ for OGLE-IV events and their corresponding error bars.

same events found by both surveys. For *Gaia*, we used the `paczynski1_te` parameter derived in the model with blending, as the OGLE timescales were also derived using a blended model. We note that the amount of blending seen in a ground-based survey should typically be greater than in a space-based survey such as *Gaia*; however, we assume that the microlensing model with blending yields the actual event timescale, which does not depend on blending. On the other hand, sparse *Gaia* light curves might not be the best suited for obtaining robust measurements of the amount of blending. Indeed, most of the measurements with $t_E > 100$ days that are outlying from the one-to-one relation to OGLE timescales in Figure 16 are fairly short-lasting events, but their blending, as derived from sparse *Gaia* data, was estimated to be high ($f_s \ll 1$). Highly blended solutions should always be treated with caution and we recommend a more detailed study of these events and their light curves.

In general, the comparison of timescales reveals good agreement with the measurements of OGLE, especially for the brighter sample with $G_0 < 19$ mag (primarily Sample A). The events from the disc show better correspondence than events from the bulge, primarily thanks to better cadence in *Gaia* observations of the disc fields. In a couple of cases, it can be seen that the error bars on the timescales of *Gaia* events are clearly underestimated. Typically, the timescale errors are about 7 days,

but they span to 70 days in the case of Level 0, and up to 300 for Level 1, owing to the fact that the more complex blended model is less constrained by the sparse light curves of *Gaia*.

6.3. Contamination

Microlensing events were identified in the *Gaia* DR3 data solely based on the shape of their light curves and the colours of the source star. In future *Gaia* data releases, when astrometric time-series become available, it will also be possible to recognise microlensing events as an astrometric deviation due to lensing (Dominik & Sahu 2000; Belokurov & Evans 2002; Rybicki et al. 2018). Until then, we have to rely on photometry only. The contamination with non-microlensing events, which can mimic the shape of the microlensing light curve, is particularly possible in the case of sparsely sampled light curves such as those from *Gaia*. The contamination with non-microlensing variables is mostly going to affect our Sample A, as this latter was obtained in an automated fashion. Sample B is composed of previously known and published microlensing events, and therefore their reliability is greater. As the events reported here are concentrated very near the Galactic plane (to within $\pm 20^\circ$), the main types of contaminants will be of Galactic origin.

Nevertheless, we identified one candidate, #257, 3388787058343659648, in common with a list of candidate quasi-stellar objects (QSOs; or ‘quasars’) from Shu et al. (2019), who used *Gaia* DR2 and AllWISE data to identify potential QSOs without knowledge of their light curves. The photometric evolution of this event clearly shows a slow rise with the amplitude of about 0.8 mag, but the event is not covered until the brightness returns to quiescence. Additional observations of this source from CRTS (Drake et al. 2009), covering about 8 years before *Gaia* started, show a flat light curve. Similarly, ZTF data from 3 years after *Gaia* also show a flat light curve, while for a QSO we might have expected at least low-level long-term variability. Further studies and future *Gaia* data are necessary to distinguish between the microlensing and QSO nature of this source.

In a subsequent step, we cross-matched our candidate events with the catalogue of variables from OGLE, in particular the catalogue of nearly 250 000 long-period variables (LPVs), which show slowly varying large-amplitude periodic or semi-periodic variations in their light curves (Soszyński et al. 2013). There was one object in common with our catalogue, namely event #004 (4043236380953360512), which matched to OGLE-BLG-LPV-102568, and was identified from the OGLE light curve as an (OGLE small-amplitude red giant (OSARG; Wray et al. 2004)-type variable. OSARGs are known for their small amplitudes, while here the event shows a very significant change in brightness of about 1 mag. We suggest that #004 is a genuine microlensing event, in which the source happened to be a variable star of the OSARG type. Such events are fairly rare, but most often are just not being detected due to the prior variability in their baselines (but see Wyrzykowski et al. (2006)). This event was also not detected by any survey other than *Gaia*, most likely because of the prior baseline variability, despite its high brightness and high amplitude. A very similar case is presented below in Section 6.4, where a baseline variation of small amplitude is superimposed with the microlensing event (event #007).

The cross-match of microlensing events with the *Gaia* DR2 catalogue of 550 000 variable star candidates (Mowlavi et al. 2018) yielded another match, #066 (4048971261782646528), classified in *Gaia* DR2 as a potential LPV. The *Gaia* DR3 light curve indeed shows a red variable object, but with an amplitude

of nearly 2 mag and a non-repeating shape of the outburst; we suggest this again is a genuine microlensing event. The classification in *Gaia* DR2 relied on a much shorter light curve and therefore an event without its full baseline could have fallen into the LPV selection. We note that this source is no longer considered as an LPV candidate in the newest DR3 LPV catalogue (Lebzelter et al. 2022).

Microlensing events can also be mimicked by other types of variable stars, with the main ones being Be-type outbursts (Mennickent et al. 2003; Sabogal et al. 2005; Keller et al. 2002; Rivinius et al. 2013), cataclysmic variables (CVs; Downes et al. (1997)), and YSOs (Andre & Montmerle 1994; Marton et al. 2019). Automated ways to distinguish microlensing events from those common contaminants were recently discussed by Godines et al. (2019) and Gezer et al. (2022).

We used Simbad² in order to identify any potential overlaps additional classes. We found two candidates, #002, 4135677580466393216 and #051, 443788525336160512, marked as potential LPVs in the catalogue of variable stars from the ATLAS survey (Heinze et al. 2018). However, as the ATLAS data used for the classification spanned only two years and microlensing events were not considered in their search, we suspect these two events were incorrectly identified as LPVs and are actually microlensing events given the shape of their light curves and good matches to the microlensing models in *Gaia* DR3 data.

Another event, #137 (3012224323198211968), was classified as a potential YSO by Großschedl et al. (2019) based on its VISTA/WISE archival observations. The *Gaia* light curve shows a double-peaked event, which can also be explained by a strong microlensing parallax. Such photometric behaviour is not uncommon in YSOs, but there is also a chance of microlensing occurring on a young and dusty star. Moreover, both CRTS and ZTF observations prior to and following the event show no further brightening episodes, which would be expected if the source were a YSO variable star. Further observations and a longer *Gaia* light curve are necessary to verify the nature of this event.

One of our events, #118, 3355845866073702144, which was also discovered in real time as a transient by the ASAS-SN survey (Shappee et al. 2014) and dubbed ASASSN16-li, was marked as a candidate cataclysmic variable on the ASAS-SN web page³. This transient was also detected by the OGLE disk survey (Mróz et al. 2020b) as a potential (but weak) microlensing candidate. Both ASAS-SN and OGLE light curves cover the transient very sparsely, in particular, the pre-peak part of the event is not covered at all, hence the suspicion of a CV. Cataclysmic variables typically show a fast-rise-exponential-decline (FRED)-type light curve. *Gaia* data contain only one data point prior to the peak of the event, and so cannot be used to rule out the FRED shape. However, the long-term ASAS-SN and OGLE data do not show any other outbursts, as are typically seen in most CVs. We suspect that this is a genuine microlensing event that was mistaken for a CV because of the sparse sampling, because to our knowledge no spectroscopic classification was performed.

Relying on photometry only, we can use the known fact that microlensing events do not repeat. In the history of microlensing, so far the only few cases of repeating microlensing events were found when the lens was a very wide binary system or a planetary system and the lensing episodes were separated by 1-2 years (Skowron et al. 2009; Poleski et al. 2014). Therefore,

² <http://simbad.u-strasbg.fr/simbad/>

³ <https://www.astronomy.ohio-state.edu/asassn/transients.html>

for our sample we can assume they should not show any further brightening episodes after the event. Repeating Galactic transients that could mimic microlensing are primarily CVs, YSOs, and Be-type outbursts. Here, we searched for outbursts reported some time after the end of *Gaia* DR3 (from mid-2018) in surveys monitoring the sky where *Gaia* microlensing events are located. We searched among alerts from *Gaia* itself, the *Gaia* Science Alerts (Hodgkin et al. 2021), and found zero matches. The search among OGLE microlensing candidates from bulge and disc (Mróz et al. 2019, 2020b) also yielded no matches. We also checked the microlensing catalogue from ZTF, which started operating after 2018 (Rodríguez et al. 2021; Medford et al. 2022), and again found no matches to our events. We also extracted photometry from ZTF DR9⁴ (Masci et al. 2019) and visually inspected all light curves with ZTF data covering the years 2018-2022. No variability or additional outbursts were found, lowering the chance that there are non-microlensing events within our sample.

In summary, we cross-matched *Gaia* microlensing events with known types of variables and potential repeaters and found six matches in total with objects also classified as LPVs, QSOs, YSOs, and a CV. We are confident that four events matching the LPVs and a CV are actually genuine microlensing events, while the remaining two matches still have to be confirmed. With 363 events in total in our catalogue, the contamination is therefore estimated to 0.6% (for two contaminants) and 1.7% (for six contaminants). We note the contamination rate can be higher as we only explored a limited range of possible types of contaminants.

6.4. Individual cases

As listed in Table E.1, 273 of 363 events in our catalogue have been independently identified by other large-scale surveys. Additionally, many of the sources with events identified during *Gaia* DR3 and found only by *Gaia* were located in the fields monitored by various large-sky surveys after the event. As discussed above, publicly available ASAS-SN and ZTF time-series were used in particular to check for any potential secondary outbursts and to rule out non-microlensing variable stars. Below, we discuss selected cases of events from our catalogue and show the microlensing model fit to the *Gaia* data combined with publicly available data from other surveys.

The first example and the first entry in our catalogue, GaiaDR3-ULENS-001 (sourceid=6059400613544951552), has only *Gaia* data during the event. Figure 17 shows *Gaia* G , G_{BP} , and G_{RP} data for event #001 which had a baseline magnitude of $G = 13.58$ mag, and was located in the Galactic disc at the Galactic longitude of 298° . This part of the sky has also been monitored by OGLE and ASAS-SN, but neither of these surveys reported any transient at that location when it occurred in mid-2015. Later publicly available ASAS-SN data show no variation in brightness. The light curve in all *Gaia* bands was modelled using the MulensModel open source code (Poleski & Yee 2019) and three different models were fit. The standard model with blending is clearly not reproducing many of the data points, while the model with annual microlensing parallax fits the data much better. The figure also shows a comparison of the parallax model with and without the inclusion of the space parallax due to the Earth-*Gaia* distance. The space parallax is negligible for event #001.

⁴ <https://www.ztf.caltech.edu/ztf-public-releases.html>

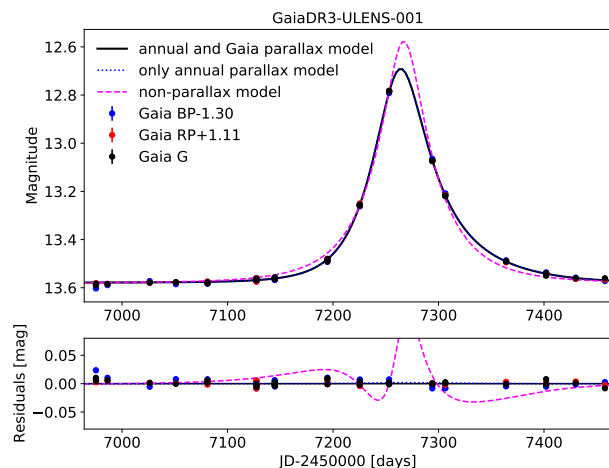


Fig. 17. Data, models, and their residuals for GaiaDR3-ULENS-001 event, Gaia sourceid=6059400613544951552. Data error bars are smaller than the size of the marker. A standard microlensing model with blending is shown with the magenta dashed line, a model with annual parallax without space parallax is shown with a blue dotted line, while the black line shows the annual parallax model with *Gaia* space parallax effect. Models were obtained using the MulensModel code (Poleski & Yee 2019).

Event #001 is an example of a microlensing event found in *Gaia* DR3 data but previously missed by other surveys looking for microlensing events in the southern hemisphere. Such a bright event would have benefited from more detailed light curve coverage as well as spectroscopy in order to derive its microlensing parameters. In the case of such a bright event, the *Gaia* astrometric measurements are expected to have accuracy of better than 1 mas (Rybcicki et al. 2018). This event will therefore be a perfect case study for future astrometric microlensing signal searches using *Gaia*'s superb astrometric time series.

Figure 18 shows event GaiaDR3-ULENS-002 with *Gaia* sourceid=4135677580466393216. This star was previously classified as a LPV by the ATLAS survey (Heinze et al. 2018). Additional observations of the ZTF survey collected in the years 2018-2022, and therefore well after the increase in brightness, show no further large-scale variability, as would usually be expected for LPVs. This confirms that event #002 is most likely a genuine microlensing event.

The next example we wish to present is GaiaDR3-ULENS-007 (*Gaia* sourceid=4042926314286962944). Figure 19 shows *Gaia* G , G_{BP} , and G_{RP} data points together with the OGLE-IV data from their Early Warning System (Udalski et al. 2015), where its designation is OGLE-2015-BLG-0064. The standard microlensing model fit to both *Gaia* and OGLE data is also shown with its residuals at the bottom. We note that there is low-level variability present in the OGLE I-band data that is visible before and during the event. According to the study of variable baseline microlensing events by Wyrzykowski et al. (2006), the change in the amplitude of the variation is related to the blending parameter and could indicate whether the variability comes from the source or the blend (including the lens). In case of a non-blended varying source, the variability amplitude should not change while amplified, but in the case of a strongly blended varying source, the observed amplitude should increase. In an opposite case of a variable blend (or lens), the variation amplitude should decrease with increasing magnification of the

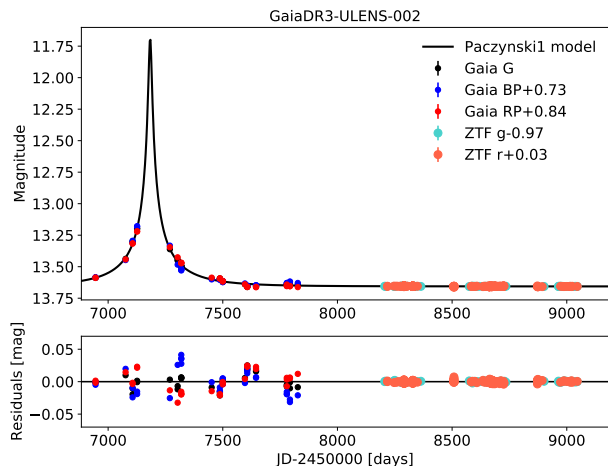


Fig. 18. Data, Level 1 model, and its residuals for event GaiaDR3-ULENS-002/4135677580466393216, previously classified as a candidate LPV by the ATLAS survey. Data from the ZTF survey collected well after the event do not show any additional variability, which would usually be expected for a LPV star.

source. In the case of GaiaDR3-ULENS-007/OGLE-2015-BLG-0064, the baseline amplitude is very small, of about 0.02 mag (peak-to-peak). The blending parameter obtained in the Level 1 fit for *Gaia* data only was about 0.12 in *G*. For the *Gaia*-OGLE combined data set, we again used *MulensModel* (Poleski & Yee 2019) and obtained a blending parameter of about 0.3 for *G* and the OGLE I-band. If the source is variable and is contributing as little as 12%-30% of the light at the baseline, its variability amplitude should increase to about 0.03 mag if we take the microlensing amplification of about two in this case. The observed amplitude during the event, seen more clearly in the residuals, is indeed somewhat larger, suggesting the source in this event is variable and its fully de-blended variation amplitude should be about 0.07 mag, as typically seen in OSARGs (Wray et al. 2004; Soszyński et al. 2009, 2013). The red colour and bright magnitude of #007, even after de-blending, is also consistent with the red giant star in the bulge, a location where many of the microlensing sources can be found. In the case of a variable blend, the variability amplitude in this event (assuming $A \sim 2$ obtained from the standard microlensing model) would decrease to about 0.01 mag. In fact, the irregularity of the variations makes it hard to measure the amplitude precisely, but we suspect the varying source scenario is more probable here.

There are seven microlensing events in our catalogue, which were alerted in near-real-time by the GSA system (Hodgkin et al. 2021). Figure 20 shows one of them, Gaia17aqu (or simply ‘Aqua’). The event was also discovered in a dedicated search for microlensing events in the OGLE-IV Galactic disc fields by Mróz et al. (2020b) and the OGLE I-band data are also shown in Figure 20. *Gaia* DR3 data as well as those of OGLE cover only the rising part of the event, while GSA data⁵ cover also the declining part of the light curve. The Level 1 Paczynski model (with blending) is shown in the figure and it reproduces all data sets well with the timescale of about 100 days.

A long-lasting microlensing event, called ASASSN-16oe, was discovered in real-time by the ASAS-SN survey (Shappee et al. 2014) in 2016, which is within the time-span of *Gaia*

⁵ <https://gsaweb.ast.cam.ac.uk/alerts/alert/Gaia17aqu>

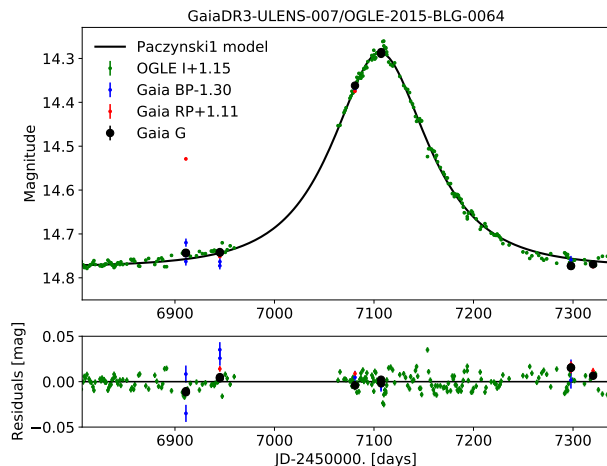


Fig. 19. Data, microlensing model, and its residuals for event GaiaDR3-ULENS-007, *Gaia* sourceid=4042926314286962944. This event was also discovered in real-time by the OGLE-IV survey as OGLE-2015-BLG-0064. The OGLE data clearly show low-level irregular variability due to either source or lens variability.

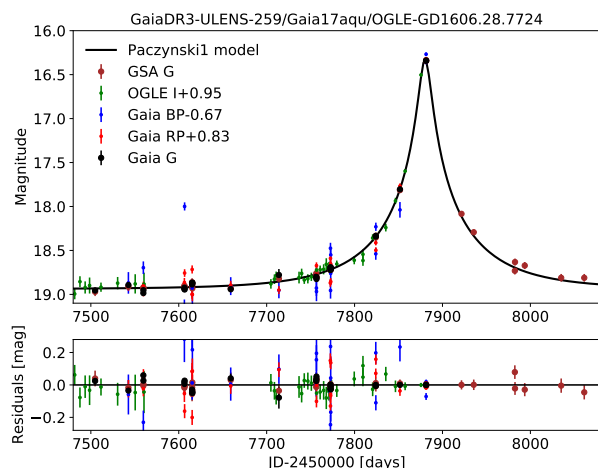


Fig. 20. Data, the Level 1 microlensing model, and its residuals for event GaiaDR3-ULENS-259, *Gaia* sourceid=5599913394301352832. This event was discovered while ongoing by the GSA system as Gaia17aqu, and was also found by the OGLE survey.

DR3 data collection. The source observed by *Gaia* (sourceid=6059816980526317568) contained the microlensing event and was also detected by the OGLE survey (Mróz et al. 2020b). This source was added to our Sample B and the event was dubbed GaiaDR3-ULENS-023. Figure 21 shows the data from all surveys together with the parallax and standard models and their residuals obtained using *MulensModel* (Poleski & Yee 2019). A simple parallax model fit to all the available data (*Gaia*, ASAS-SN, OGLE) yielded a good fit with the heliocentric timescale of about 177 days, blending in *G* of about 0.65, and a length of the microlensing parallax vector of $\pi_E = 0.18$. Those values, combined in Equation 7 with $\theta_E = t_E/\mu_{rel}$ and a typical value of relative source–lens proper motion of $\mu_{rel} \sim 3$ mas/yr, yield a mass for the lens of about $1 M_\odot$ located at 2.5 kpc, if the source distance is assumed to be 8 kpc. Because of a high

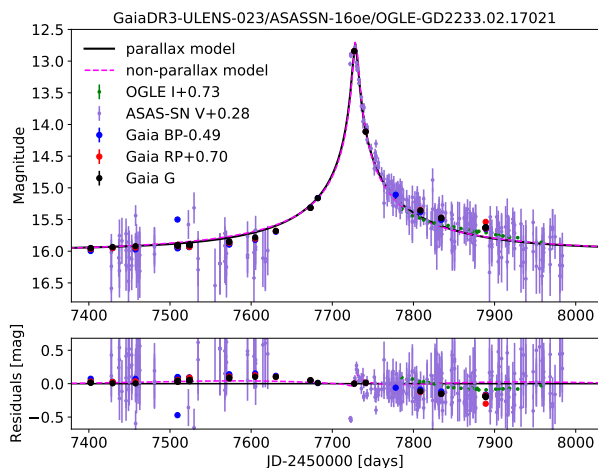


Fig. 21. Data, microlensing models, and their residuals for event GaiaDR3-ULENS-023, *Gaia* sourceid=6059816980526317568. This event was discovered while ongoing by the ASAS-SN survey as ASASSN-16oe, and was also found by the OGLE survey. The microlensing models were obtained with the *MulensModel* code.

level of blending in this event, the lens can be explained with a regular main sequence star yielding all the blended light at that distance. A more detailed study is necessary in order to establish the most probable mass and distance of the lens (e.g. Wyrzykowski et al. 2016; Wyrzykowski & Mandel 2020; Mróz & Wyrzykowski 2021). However, in the case of this bright and long-lasting event, the actual mass and distance of the lens measurement should be possible with the use of the forthcoming *Gaia* astrometric time series (Rybicki et al. 2018).

7. Summary

We present the first catalogue of *Gaia* microlensing events from all over the sky. We find 363 unique events, of which 90 have not previously been reported. *Gaia* DR3 contains complete light curves in G , G_{BP} , and G_{RP} *Gaia* bands as well as the parameters of microlensing models from Level 0 and Level 1 fits. The catalogue is far from complete, as the relatively short time-span of the data (2014–2017) and a very large starting number of sources to investigate (~ 2 billion) required a very conservative approach in the search for potential microlensing events. The completeness, derived by comparison to the OGLE-IV results, is at a level of 30% for the bulge region and up to 80% in the disc regions for the brighter end of the sample. Our catalogue is also fairly complete for events with timescales longer than about 60 days, in particular in the disc regions. On the other hand, contamination of the catalogue is estimated to a very low level of below 1%.

The catalogue can be used in further statistical studies of the distribution of microlensing events in the Galaxy as well as for individual studies searching for black hole or planetary lenses. Some of the events at the time of publication are already 8 years old and can be targeted with high-resolution observations in order to see the source and lens separated, provided their relative proper motion is high (e.g. Kozłowski et al. 2007; Abdurrahman et al. 2021). The remaining events will also be suitable for such studies within the next 5–10 years.

Many of the microlensing events found in *Gaia* were also found by other surveys. The potential further work includes more

detailed modelling of the *Gaia* and other data combined, with the inclusion of the annual and space microlensing parallax. Such studies could lead to the identification of potential dark lenses, including black holes and neutron stars (e.g. Mao et al. 2002; Bennett et al. 2002; Wyrzykowski et al. 2016; Mróz & Wyrzykowski 2021).

Future *Gaia* data releases will provide more photometric observations of the events published here, as well as new events from a much longer time baseline. Moreover, *Gaia* astrometric time-series available for photometrically identified microlensing events will yield complete solutions for lens masses and distances, and discoveries of dozens of black holes and neutron stars in the Milky Way. When combined with other *Gaia* data products, such as colour light curves, low-resolution spectroscopic time-series, and radial velocity measurements, *Gaia* will revolutionise studies of the populations of lenses in the Galaxy.

Acknowledgements. This work has made use of data from the European Space Agency (ESA) mission *Gaia* (<https://www.cosmos.esa.int/gaia>), processed by the *Gaia* Data Processing and Analysis Consortium (DPAC, <https://www.cosmos.esa.int/web/gaia/dpac/consortium>). Funding for the DPAC has been provided by national institutions, some of which participate in the *Gaia* Multilateral Agreement, which include, for Switzerland, the Swiss State Secretariat for Education, Research and Innovation through the ESA Prodex program, the ‘Mesures d’accompagnement’, the ‘Activités Nationales Complémentaires’, the Swiss National Science Foundation, and the Early Postdoc.Mobility fellowship; for Belgium, the BELgian federal Science Policy Office (BELSPO) through PRODEX grants; for Italy, Istituto Nazionale di Astrofisica (INAF) and the Agenzia Spaziale Italiana (ASI) through grants I/037/08/0, I/058/10/0, 2014-025-R.0, and 2014-025-R.1.2015 to INAF (PI M.G. Lattanzi); for Hungary, the Lendület grants LP2014-17 and LP2018-7 from the Hungarian Academy of Sciences, and the NKFIH grants K-115709, PD-116175, PD-121203 from the Hungarian National Research, Development, and Innovation Office. L.W., K.K. and K.A.R. have been supported by the Polish National Science Centre (NCN) grants Harmonia No. 2018/30/M/ST9/00311 and Daina No. 2017/27/L/ST9/03221 as well as the European Union’s Horizon 2020 research and innovation programme under grant agreement No 101004719 (OPTICON-RadioNet Pilot, ORP) and MNiSW grant DIR/WK/2018/12. L.M. and E.P. have been supported by the János Bolyai Research Scholarship of the Hungarian Academy of Sciences. We would like to thank the OGLE team for making their data and statistics available to the public. We also thank numerous researchers and students involved in *Gaia* microlensing studies, whose comments and discussions helped in this work, in particular to Andrzej Udalski, Przemek Mróz, Radek Poleski, Jan Skowron, Paweł Zieliński, Mariusz Gromadzki, Maja Jabłońska, Piotr Trzcionkowski. This work made use of software from Postgres-XL (<https://www.postgres-xl.org>), Java (<https://www.oracle.com/java/>), R (R Core Team 2018), and TOPCAT/STILTS (Taylor 2020, 2019, 2017, 2005). This research has made use of the SIMBAD database, operated at CDS, Strasbourg, France (Wenger et al. 2000).

References

- Abbott, R., Abbott, T. D., Abraham, S., et al. 2021, *ApJ*, 913, L7
 Abdurrahman, F. N., Stephens, H. F., & Lu, J. R. 2021, *ApJ*, 912, 146
 Abe, F., Allen, W., Banks, T., et al. 1997a, in *Variables Stars and the Astrophysical Returns of the Microlensing Surveys*, ed. R. Ferlet, J.-P. Maillard, & B. Raban, 75
 Abe, F., Allen, W., Banks, T., et al. 1997b, in *Variables Stars and the Astrophysical Returns of the Microlensing Surveys*, ed. R. Ferlet, J.-P. Maillard, & B. Raban, 75
 Afonso, C., Albert, J. N., Alard, C., et al. 2003, *A&A*, 404, 145
 Alcock, C., Akerlof, C. W., Allsman, R. A., et al. 1993, *Nature*, 365, 621
 Alcock, C., Allsman, R. A., Alves, D., et al. 1997, *ApJ*, 486, 697
 Alcock, C., Allsman, R. A., Alves, D. R., et al. 2001a, *Astrophysical Journal Letters*, 550, L169
 Alcock, C., Allsman, R. A., Alves, D. R., et al. 2000, *ApJ*, 542, 281
 Alcock, C., Allsman, R. A., Alves, D. R., et al. 2001b, *Nature*, 414, 617
 Alcock, C., Allsman, R. A., Axelrod, T. S., et al. 1996, *ApJ*, 461, 84
 Alcock, C., Axelrod, T. S., Bennett, D. P., et al. 1992, in *Astronomical Society of the Pacific Conference Series*, Vol. 103, *Robotic Telescopes in the 1990s*, ed. A. V. Filippenko, 193–202
 An, J. H., Albrow, M. D., Beaulieu, J. P., et al. 2002, *ApJ*, 572, 521
 Andre, P. & Montmerle, T. 1994, *ApJ*, 420, 837
 Aubourg, E., Bareyre, P., Brehin, S., et al. 1993, *The Messenger*, 72, 20

- Awiphan, S., Kerins, E., & Robin, A. C. 2016, *MNRAS*, 456, 1666
- Bachelet, E., Zieliński, P., Gromadzki, M., et al. 2022, *A&A*, 657, A17
- Bailer-Jones, C. A. L., Rybizki, J., Fouesneau, M., Demleitner, M., & Andrae, R. 2021, *AJ*, 161, 147
- Batista, V., Gould, A., Dieters, S., et al. 2011, *A&A*, 529, A102
- Beaulieu, J. P., Bennett, D. P., Fouqué, P., et al. 2006, *Nature*, 439, 437
- Bekki, K. 2009, *MNRAS*, 398, L36
- Bellm, E. C., Kulkarni, S. R., Graham, M. J., et al. 2019, *PASP*, 131, 018002
- Belokurov, V., Penoyre, Z., Oh, S., et al. 2020, *MNRAS*, 496, 1922
- Belokurov, V. A. & Evans, N. W. 2002, *MNRAS*, 331, 649
- Bennett, D. P. 2005, *ApJ*, 633, 906
- Bennett, D. P., Akerlof, C., Alcock, C., et al. 1993, in *Texas/PASCOS '92: Relativistic Astrophysics and Particle Cosmology*, ed. C. W. Akerlof & M. A. Srednicki, Vol. 688, 612
- Bennett, D. P., Becker, A. C., Quinn, J. L., et al. 2002, *ApJ*, 579, 639
- Bennett, D. P., Ranc, C., & Fernandes, R. B. 2021, *Astronomical Journal*, 162, 243
- Bird, S., Cholis, I., Muñoz, J. B., et al. 2016, *Phys. Rev. Lett.*, 116, 201301
- Bond, I. A., Abe, F., Dodd, R. J., et al. 2001, *MNRAS*, 327, 868
- Bond, I. A., Udalski, A., Jaroszyński, M., et al. 2004, *ApJ*, 606, L155
- Carr, B., Kühnel, F., & Sandstad, M. 2016, *Phys. Rev. D*, 94, 083504
- Carr, B. J. 1975, *ApJ*, 201, 1
- Cassan, A., Kubas, D., Beaulieu, J. P., et al. 2012, *Nature*, 481, 167
- Cassan, A., Ranc, C., Absil, O., et al. 2022, *Nature Astronomy*, 6, 121
- Derue, F., Afonso, C., Alard, C., et al. 2001, *A&A*, 373, 126
- Dominik, M. & Sahu, K. C. 2000, *ApJ*, 534, 213
- Dong, S., Mérand, A., Delplancke-Ströbele, F., et al. 2019, *ApJ*, 871, 70
- Downes, R., Webbink, R. F., & Shara, M. M. 1997, *PASP*, 109, 345
- Drake, A. J., Djorgovski, S. G., Mahabal, A., et al. 2009, *ApJ*, 696, 870
- Einstein, A. 1936, *Science*, 84, 506
- Evans, N. W. & Belokurov, V. 2002, *ApJ*, 567, L119
- Eyer et al. 2022, *A&A* in prep.
- Fabircius, C., Luri, X., Arenou, F., et al. 2021, *A&A*, 649, A5
- Fukui, A., Suzuki, D., Koshimoto, N., et al. 2019, *AJ*, 158, 206
- Gaia Collaboration. 2022, *A&A* in prep.
- Gaia Collaboration, Prusti, T., de Bruijne, J. H. J., et al. 2016, *A&A*, 595, A1
- García-Bellido, J. & Ruiz Morales, E. 2017, *Physics of the Dark Universe*, 18, 47
- Gaudi, B. S., Patterson, J., Spiegel, D. S., et al. 2008, *ApJ*, 677, 1268
- Gezer, I., Wyrzykowski, Ł., Zieliński, P., et al. 2022, arXiv e-prints, arXiv:2201.12209
- Godines, D., Bachelet, E., Narayan, G., & Street, R. A. 2019, *Astronomy and Computing*, 28, 100298
- Gould, A. 2000, *ApJ*, 542, 785
- Gould, A. 2004, *ApJ*, 606, 319
- Großschedl, J. E., Alves, J., Teixeira, P. S., et al. 2019, *A&A*, 622, A149
- Han, C. 2008, *ApJ*, 681, 806
- Heinze, A. N., Tonry, J. L., Denneau, L., et al. 2018, *AJ*, 156, 241
- Hodgkin, S. T., Harrison, D. L., Breedt, E., et al. 2021, arXiv e-prints, arXiv:2106.01394
- Jayasinghe, T., Kochanek, C. S., Stanek, K. Z., et al. 2017, *The Astronomer's Telegram*, 10677, 1
- Kains, N., Calamida, A., Sahu, K. C., et al. 2017, *ApJ*, 843, 145
- Keller, S. C., Bessell, M. S., Cook, K. H., Geha, M., & Syphers, D. 2002, *AJ*, 124, 2039
- Kerins, E., Robin, A. C., & Marshall, D. J. 2009, *MNRAS*, 396, 1202
- Kim, S.-L., Lee, C.-U., Park, B.-G., et al. 2016, *Journal of Korean Astronomical Society*, 49, 37
- Kiraga, M. & Paczynski, B. 1994, *ApJ*, 430, L101
- Klüter, J., Bastian, U., Demleitner, M., & Wambsganss, J. 2018, *A&A*, 620, A175
- Kozłowski, S., Woźniak, P. R., Mao, S., & Wood, A. 2007, *ApJ*, 671, 420
- Kruszyńska, K., Wyrzykowski, Ł., Rybicki, K. A., et al. 2022, *A&A*, 662, A59
- Lam, C. Y., Lu, J. R., Udalski, A., et al. 2022, *ApJ*, 933, L23
- Lebzelter et al. 2022, *A&A* in prep.
- Lindgren, L., Bastian, U., Biermann, M., et al. 2021, *A&A*, 649, A4
- Mao, S. & Paczynski, B. 1991, *ApJ*, 374, L37
- Mao, S., Smith, M. C., Woźniak, P., et al. 2002, *MNRAS*, 329, 349
- Marton, G., Ábrahám, P., Szegedi-Elek, E., et al. 2019, *MNRAS*, 487, 2522
- Masci, F. J., Laher, R. R., Rusholme, B., et al. 2019, *PASP*, 131, 018003
- Medford, M. S., Lu, J. R., Nugent, P., & Lam, C. Y. 2022, arXiv e-prints, arXiv:2201.08335
- Mennickent, R. E., Pietrzyński, G., & Gieren, W. 2003, in *Astronomical Society of the Pacific Conference Series*, Vol. 292, *Interplay of Periodic, Cyclic and Stochastic Variability in Selected Areas of the H-R Diagram*, ed. C. Sterken, 89
- Mowlavi, N., Lecoœur-Taïbi, I., Lebzelter, T., et al. 2018, *A&A*, 618, A58
- Mróz, P., Ryu, Y. H., Skowron, J., et al. 2018, *AJ*, 155, 121
- Mróz, P., Street, R. A., Bachelet, E., et al. 2020a, *Research Notes of the American Astronomical Society*, 4, 13
- Mróz, P., Udalski, A., Skowron, J., et al. 2017, *Nature*, 548, 183
- Mróz, P., Udalski, A., Skowron, J., et al. 2019, *ApJS*, 244, 29
- Mróz, P., Udalski, A., Szymański, M. K., et al. 2020b, *ApJS*, 249, 16
- Mróz, P. & Wyrzykowski, Ł. 2021, *Acta Astron.*, 71, 89
- Munari, U., Hamsch, F. J., & Frigo, A. 2016, *The Astronomer's Telegram*, 9879, 1
- Navarro, M. G., Contreras Ramos, R., Minniti, D., et al. 2020a, *ApJ*, 893, 65
- Navarro, M. G., Minniti, D., Pullen, J., & Ramos, R. C. 2020b, *ApJ*, 889, 56
- Nemiroff, R. J. 1998, *ApJ*, 509, 39
- Nucita, A. A., Licchelli, D., De Paolis, F., et al. 2018, *MNRAS*, 476, 2962
- Paczynski, B. 1986, *ApJ*, 304, 1
- Paczynski, B. 1996, *ARA&A*, 34, 419
- Poleski, R., Skowron, J., Mróz, P., et al. 2021, *Acta Astron.*, 71, 1
- Poleski, R., Skowron, J., Udalski, A., et al. 2014, *ApJ*, 795, 42
- Poleski, R. & Yee, J. C. 2019, *Astronomy and Computing*, 26, 35
- Popowski, P., Alcock, C., Allsman, R. A., et al. 2001, in *Astronomical Society of the Pacific Conference Series*, Vol. 239, *Microlensing 2000: A New Era of Microlensing Astrophysics*, ed. J. W. Menzies & P. D. Sackett, 244
- R Core Team. 2018, *R: A Language and Environment for Statistical Computing*, R Foundation for Statistical Computing, Vienna, Austria
- Rahal, Y. R., Afonso, C., Albert, J. N., et al. 2009, *A&A*, 500, 1027
- Riello, M., De Angeli, F., Evans, D. W., et al. 2021, *A&A*, 649, A3
- Riviniuti, T., Carciofi, A. C., & Martayan, C. 2013, *A&A Rev.*, 21, 69
- Rodriguez, A. C., Mróz, P., Kulkarni, S. R., et al. 2021, arXiv e-prints, arXiv:2112.07684
- Rybicki, K. A., Wyrzykowski, Ł., Bachelet, E., et al. 2022, *A&A*, 657, A18
- Rybicki, K. A., Wyrzykowski, Ł., Klencki, J., et al. 2018, *MNRAS*, 476, 2013
- Rybizki, J., Green, G. M., Rix, H.-W., et al. 2022, *MNRAS*, 510, 2597
- Sabogal, B. E., Mennickent, R. E., Pietrzyński, G., & Gieren, W. 2005, *MNRAS*, 361, 1055
- Sahu, K. C. 1994, *Nature*, 370, 275
- Sahu, K. C., Anderson, J., Casertano, S., et al. 2017, *Science*, 356, 1046
- Sahu, K. C., Anderson, J., Casertano, S., et al. 2022, *ApJ*, 933, 83
- Sahu, K. C., Bond, H. E., Anderson, J., & Dominik, M. 2014, *ApJ*, 782, 89
- Sako, T., Sekiguchi, T., Sasaki, M., et al. 2008, *Experimental Astronomy*, 22, 51
- Shappee, B. J., Prieto, J. L., Grupe, D., et al. 2014, *ApJ*, 788, 48
- Shu, Y., Koposov, S. E., Evans, N. W., et al. 2019, *MNRAS*, 489, 4741
- Skowron, J., Udalski, A., Gould, A., et al. 2011, *ApJ*, 738, 87
- Skowron, J., Udalski, A., Kozłowski, S., et al. 2016, *Acta Astron.*, 66, 1
- Skowron, J., Wyrzykowski, Ł., Mao, S., & Jaroszyński, M. 2009, *MNRAS*, 393, 999
- Soszyński, I., Udalski, A., Szymański, M. K., et al. 2009, *Acta Astron.*, 59, 239
- Soszyński, I., Udalski, A., Szymański, M. K., et al. 2013, *Acta Astron.*, 63, 21
- Stanek, K. Z., Mateo, M., Udalski, A., et al. 1994, *ApJ*, 429, L73
- Strader, J., Chomiuk, L., Stanek, K. Z., et al. 2016, *The Astronomer's Telegram*, 9860, 1
- Sumi, T., Bennett, D. P., Bond, I. A., et al. 2013, *ApJ*, 778, 150
- Sumi, T., Kamiya, K., Bennett, D. P., et al. 2011, *Nature*, 473, 349
- Suzuki, D., Bennett, D. P., Sumi, T., et al. 2016, *Astrophysical Journal*, 833, 145
- Taylor, D. K., Dickman, R. L., & Scoville, N. Z. 1987, *ApJ*, 315, 104
- Taylor, M. 2017, arXiv e-prints, arXiv:1707.02160
- Taylor, M. 2020, arXiv e-prints, arXiv:2012.10560
- Taylor, M. B. 2005, in *Astronomical Society of the Pacific Conference Series*, Vol. 347, *Astronomical Data Analysis Software and Systems XIV*, ed. P. Shopbell, M. Britton, & R. Ebert, 29
- Taylor, M. B. 2019, in *Astronomical Society of the Pacific Conference Series*, Vol. 523, *Astronomical Data Analysis Software and Systems XXVII*, ed. P. J. Teuben, M. W. Pound, B. A. Thomas, & E. M. Warner, 43
- Tisserand, P., Le Guillou, L., Afonso, C., et al. 2007, *A&A*, 469, 387
- Udalski, A., Jaroszyński, M., Paczyński, B., et al. 2005, *ApJ*, 628, L109
- Udalski, A., Szymanski, M., Kaluzny, J., et al. 1993, *Acta Astron.*, 43, 289
- Udalski, A., Szymanski, M., Kaluzny, J., Kubiak, M., & Mateo, M. 1992, *Acta Astron.*, 42, 253
- Udalski, A., Szymanski, M., Stanek, K. Z., et al. 1994a, *Acta Astron.*, 44, 165
- Udalski, A., Szymanski, M., Stanek, K. Z., et al. 1994b, *Acta Astron.*, 44, 165
- Udalski, A., Szymański, M. K., & Szymański, G. 2015, *Acta Astron.*, 65, 1
- von Neumann, J. 1941, *The Annals of Mathematical Statistics*, 12, 367
- Wegg, C., Gerhard, O., & Portail, M. 2016, *MNRAS*, 463, 557
- Wenger, M., Ochsenbein, F., Egret, D., et al. 2000, *A&AS*, 143, 9
- Wiktorowicz, G., Wyrzykowski, Ł., Chruslinska, M., et al. 2019, *ApJ*, 885, 1
- Wood, A. & Mao, S. 2005, *MNRAS*, 362, 945
- Woźniak, P. R. 2000, *Acta Astron.*, 50, 421
- Wray, J. J., Eyer, L., & Paczyński, B. 2004, *MNRAS*, 349, 1059
- Wyrzykowski, Ł., Kostrzewa-Rutkowska, Z., Skowron, J., et al. 2016, *MNRAS*, 458, 3012
- Wyrzykowski, Ł., Kozłowski, S., Skowron, J., et al. 2010, *MNRAS*, 407, 189
- Wyrzykowski, Ł., Kozłowski, S., Skowron, J., et al. 2009, *MNRAS*, 397, 1228
- Wyrzykowski, Ł., Kozłowski, S., Skowron, J., et al. 2011a, *MNRAS*, 413, 493
- Wyrzykowski, Ł. & Mandel, I. 2020, *A&A*, 636, A20
- Wyrzykowski, Ł., Mróz, P., Rybicki, K. A., et al. 2020, *A&A*, 633, A98
- Wyrzykowski, Ł., Rynkiewicz, A. E., Skowron, J., et al. 2015, *ApJS*, 216, 12
- Wyrzykowski, Ł., Skowron, J., Kozłowski, S., et al. 2011b, *MNRAS*, 416, 2949
- Wyrzykowski, Ł., Udalski, A., Mao, S., et al. 2006, *Acta Astron.*, 56, 145
- Yoo, J., DePoy, D. L., Gal-Yam, A., et al. 2004, *ApJ*, 603, 139
- Zub, M., Cassan, A., Heyrovský, D., et al. 2011, *A&A*, 525, A15

Table A.1. Data fields available in the *vari_microlensing* table of *Gaia* DR3

source_id	unique source identifier of the microlensing event candidate
paczynski0_bp0	Level 0 G_{BP} baseline magnitude [mag]
paczynski0_bp0_error	Level 0 G_{BP} baseline magnitude error [mag]
paczynski0_chi2	Level 0 goodness of fit (χ^2)
paczynski0_chi2_dof	Level 0 reduced goodness of fit (χ^2/dof)
paczynski0_g0	Level 0 G baseline magnitude [mag]
paczynski0_g0_error	Level 0 G baseline magnitude error [mag]
paczynski0_rp0	Level 0 G_{RP} baseline magnitude [mag]
paczynski0_rp0_error	Level 0 G_{RP} baseline magnitude error [mag]
paczynski0_te	Level 0 timescale (t_E) [days]
paczynski0_te_error	Level 0 timescale (t_E) error [days]
paczynski0_tmax	Level 0 time of maximum (t_{max}) [Baricentric Julian Days-2455197.5]
paczynski0_tmax_error	Level 0 time of maximum (t_{max}) error [days]
paczynski0_u0	Level 0 impact parameter (u_0)
paczynski0_u0_error	Level 0 impact parameter (u_0) error
paczynski1_bp0	Level 1 G_{BP} baseline magnitude [mag]
paczynski1_bp0_error	Level 1 G_{BP} baseline magnitude error [mag]
paczynski1_chi2	Level 1 goodness of fit (χ^2)
paczynski1_chi2dof	Level 1 reduced goodness of fit (χ^2/dof)
paczynski1_fs_bp	Level 1 G_{BP} blending parameter
paczynski1_fs_bp_error	Level 1 G_{BP} blending parameter error
paczynski1_fs_g	Level 1 G blending parameter
paczynski1_fs_g_error	Level 1 G blending parameter error
paczynski1_fs_rp	Level 1 G_{RP} blending parameter
paczynski1_fs_rp_error	Level 1 G_{RP} blending parameter error
paczynski1_g0	Level 1 G baseline magnitude [mag]
paczynski1_g0_error	Level 1 G baseline magnitude error [mag]
paczynski1_rp0	Level 1 G_{RP} baseline magnitude [mag]
paczynski1_rp0_error	Level 1 G_{RP} baseline magnitude error [mag]
paczynski1_te	Level 1 timescale (t_E) [days]
paczynski1_te_error	Level 1 timescale (t_E) error [days]
paczynski1_tmax	Level 1 time of maximum (t_{max}) [Baricentric Julian Days-2455197.5]
paczynski1_tmax_error	Level 1 time of maximum (t_{max}) error [days]
paczynski1_u0	Level 1 impact parameter (u_0)
paczynski1_u0_error	Level 1 impact parameter (u_0) error

Appendix A: Data fields in *Gaia* DR3 for candidate microlensing events.

Table A.1 describes all data fields available in table *vari_microlensing* of *Gaia* DR3 for microlensing event candidates.

Appendix B: Example of *Gaia* Archive queries

This section describes queries in ADQL that can be used to obtain different data sets using the *vari_microlensing* catalogue. More examples of queries can be found here: <https://www.cosmos.esa.int/web/gaia-users/archive/writing-queries#ADQLQueryExamples>.

Example 1, the entire catalogue

The following query will download all of the 363 sources with their equatorial and Galactic coordinates, proper motions, and ruwe along with parameters of the best microlensing model fits for Level 0 and Level 1.

```

SELECT
s.source_id, s.ra, s.dec,
s.l, s.b,
s.pmra, s.pmra_error,
s.pmdec, s.pmdec_error,
s.ruwe,
m.*
FROM gaiaedr3.gaia_source s
INNER JOIN gaiadr3.vari_microlensing m
ON s.source_id = m.source_id

```

Example 2, sources located in the Galactic bulge

The following query will download all of the sources located only within 10° from the Galactic centre. It returns their equatorial and Galactic coordinates, proper motions, and ruwe along with parameters of the best microlensing model fits for Level 0 and Level 1.

```
SELECT
s.source_id, s.ra, s.dec,
s.l, s.b,
s.pmra, s.pmra_error,
s.pmdec, s.pmdec_error,
s.ruwe,
m.*
FROM gaiaedr3.gaia_source s
INNER JOIN gaiadr3.vari_microlensing m
ON s.source_id = m.source_id
WHERE s.l<10. OR s.l>350.
```

Example 3, sources located outside of the Galactic bulge with Einstein timescales larger than 100 days

The following query will download all of the sources located outside of the 10° from the Galactic centre with Einstein timescales of Level 0 larger than 100 days. It returns their equatorial and Galactic coordinates, proper motions, and ruwe along with parameters of the best microlensing model fits for Level 0 and Level 1.

```
SELECT
s.source_id, s.ra, s.dec,
s.l, s.b,
s.pmra, s.pmra_error,
s.pmdec, s.pmdec_error,
s.ruwe,
m.*
FROM gaiaedr3.gaia_source s
INNER JOIN gaiadr3.vari_microlensing m
ON s.source_id = m.source_id
WHERE s.l BETWEEN 10. AND 350.
AND m.paczynski0_te > 100.
```

Accessing light curves

A light curve in VOTable format for a single source can be downloaded using a DataLink service. Instructions on how to do this can be found here: <https://www.cosmos.esa.int/web/gaia-users/archive/ancillary-data>. The output table has the following columns that are of interest: source_id, band, time, mag, flux_over_error. In order to transform flux_over_error into uncertainty for a given band, multiply flux_over_error by $\frac{2.5}{m(10)}$ and then use formulae 9 and 10 from this paper (Section 3).

Appendix C: Selection of candidate microlensing events

The selection of candidate microlensing at the Microlensing SOS was done by computing membership score and by applying a set of cuts on the available parameters.

Membership score

The initial score is set to 1 and then a series of tests are performed and penalties applied accordingly:

- if the amplitude in *G*-band is smaller than 0.25 mag, the score is multiplied by 0.6,
- if the amplitude in *G*-band is between 0.25 and 0.5 mag, the score is multiplied by 0.9,
- if χ^2/dof of all fitting Levels is larger than 10, the score is multiplied by 0.5,
- if the lowest χ^2 of all fit Levels is between 3 and 10, the score is multiplied by 0.9,
- if the time of maximum t_{max} including the error bar of the model with lowest χ^2 is not between the beginning and the end of the light curve in *G*, the score is multiplied by 0.9,
- if the absolute value of the impact parameter u_0 including the error bar of the model with the lowest χ^2 is not between 0 and 1.5, the score is multiplied by 0.7,
- if the absolute value of the impact parameter u_0 including the error bar of the model with lowest χ^2 is between 0 and 0.001, the score is multiplied by 0.9,
- if the model with the lowest χ^2 has baseline magnitude G_0 below 20 mag, the score is multiplied by 0.8,
- if the Einstein time t_E including the error bar is not within 2 and 500 days, the score is multiplied by 0.2,
- if one of the parallax components is larger than 1, the score is multiplied by 0.95,
- if both of the parallax components are larger than 1, the score is multiplied by 0.9.

Table C.1. Microlensing event selection cuts for **Sample A**

cut	description
$membership\ score \geq 0.85$	membership score cut
$abs(paczynski0_u0) < 1.$	only high amplification events
$20. < paczynski0_te < 300.$	timescale should be realistic and reasonable for DR3 duration
$paczynski0_g0 < 19.$	magnitude cut
$skewness < 0.$	only events getting brighter over the baseline
$1. < (median_{BP} - median_{RP}) < 4.$ $(median < 17 \text{ and } (max - min) > 0.25)$ or $(median > 17 \text{ and } (max - min) > 0.5)$	colour cut to remove blue outburst and very red variables
$stddev_G < stddev_{RP} + 0.04$ or $number\ points_{RP} < 2$	RP light curve robustness
$paczynski0_tmax - 1 * paczynski0_te > t_min$	at least 1 timescale within the data
$extractor_number_points_in_event > 3$	more than 3 outlying points identified by the Extractor
$duration > 135$	distance in days between outlying points from Extractor
$max_sigma_in_event > 50$	“strength” of the event from Extractor
$abs(paczynski0_u0/paczynski0_u0_error) < 200$	only fits with robust $paczynski0_u0$ determination selected
$paczynski0_u0_error! = 0$ and $paczynski0_te_error > 0$	only fits with robust $paczynski0_u0$ and $paczynski0_te$ selected
$paczynski2_chi2_dof < 1.9$	goodness of the parallax fit
$abs(paczynski2_parallax_east) < 3.5$ and $abs(paczynski2_parallax_north) < 3.5$	only reasonable parallax vector selected
$(paczynski0_tmax < 6,824.5$ or $paczynski0_tmax > 7,189.5)$ and $log(abbe) < 0.8 * log(-skewness) - 0.6$ or $6,824.5 \leq paczynski0_tmax \leq 7,189.5$ and $log(abbe) < 1.2 * log(-skewness) - 0.84$	skew-Abbe selection more strict for events in a period of times with more photometric outliers

Notes. If no index is given to parameters, they refer to G light curve.

Cuts and selection

Table C.1 presents the cuts used for selecting candidate microlensing events defining the **Sample A**. The cuts were identified in an iterative way, involving visual inspection of the candidates and preserving the largest number of known microlensing events. A more detailed description of the cuts and the parameters is available in the *Gaia* DR3 Documentation.

Appendix D: List of events from *Gaia* DR3

Table D.1 contains a list of all 363 *Gaia* DR3 microlensing events, sorted by their baseline magnitude, with the brightest labelled with number 1. The table lists the *Gaia* source_Id and the alias name, following the convention GaiaDR3-ULENS-NNN. The equatorial and galactic coordinates are given, the baseline magnitude in G -band. The last column marks the method the event was found, with **A** for **Sample A**, **B** for **Sample B** and **A+B** for events from both samples (see Section 4). Data from the table are also available in the on-line version of the article.

Table D.1. *Gaia* DR3 microlensing events.

GaiADR3- ULENS-	<i>Gaia</i> DR3 sourceid	RA_{J2000} [deg]	Dec_{J2000} [deg]	Gal.long. [deg]	Gal.lat. [deg]	Baseline G [mag]	Method
001	6059400613544951552	184.4363263	-59.0294197	298.6005085	3.5586850	13.58	A
002	4135677580466393216	258.0716963	-16.8677137	6.0098740	12.9894820	13.64	A
003	4084984459435880064	284.4366819	-20.7757293	14.9165537	-10.6404670	14.16	A
004	4043236380953360512	268.4052228	-33.1237924	357.2830138	-3.6192437	14.38	A
005	4046189531753775872	276.2347519	-30.9712872	2.3615295	-8.4309626	14.40	A
006	5369575367669793536	175.9545194	-51.7786254	292.4152033	9.7070281	14.74	A
007	4042926314286962944	270.2539729	-32.6895521	358.4346692	-4.7498989	14.78	A
008	6028496189222706432	255.7845506	-31.2111200	352.9458509	6.3248291	15.00	A
009	4103350800428736384	279.8111863	-15.4369500	17.8014157	-4.3444691	15.08	A
010	4056251952898990848	269.5945985	-29.9489827	0.5437424	-2.9060128	15.16	A
011	4093461453632265600	279.0502629	-18.0503157	15.1331452	-4.8801400	15.23	A+B
012	5305778988625143296	143.5517537	-57.8164443	279.0375096	-4.4075008	15.46	A
013	4052272339270449024	274.7611076	-27.7293739	4.6769250	-5.8077405	15.53	A
014	4050176120351393792	270.6320911	-30.1235644	0.8360192	-3.7732156	15.61	B
015	4053164279372999680	276.0098469	-25.1043278	7.5357066	-5.5861482	15.67	A
016	5882824406244672256	234.7379625	-56.0303213	324.8332656	-0.4528306	15.96	A
017	4041047008398705664	267.0329353	-35.5803325	354.5860534	-3.8936482	15.97	A
018	4050208551598764032	271.1193843	-29.8161981	1.3115071	-3.9914357	16.00	A+B
019	4159994512750671232	275.9289525	-7.3020659	23.2666791	2.7836325	16.01	A
020	4067907184112930944	265.7034019	-25.5169917	2.5881853	2.3205060	16.03	A
021	4041238259061973504	264.6744198	-35.5066956	353.6436127	-2.2195980	16.06	A
022	5956630082001769984	269.5337814	-42.5974274	349.4320429	-9.0692191	16.08	A
023	6059816980526317568	191.5840141	-58.8941185	302.2714390	3.9710873	16.11	B
024	5951752068649725312	262.4024369	-46.2347526	343.6506395	-6.5542396	16.13	A
025	4108020361965432064	260.8780868	-27.3787487	358.6732768	4.9403756	16.14	A+B
026	5515709499618656768	127.4644053	-47.1922367	264.6184588	-4.7449336	16.17	A
027	4039110875886635008	271.1335543	-34.8929303	356.8557550	-6.4587185	16.25	A
028	4041760939405737344	266.8708058	-34.1758834	355.7240287	-3.0570121	16.29	A
029	4063277591626468608	271.8813320	-26.6791216	4.3856614	-3.0549313	16.32	B
030	4050909181279109888	273.1546856	-27.8870166	3.8672279	-4.6272229	16.33	B
031	4062254461725875328	270.0523139	-29.7174753	0.9422900	-3.1359064	16.33	B
032	3292310414861319936	71.4940480	8.2457040	189.7124147	-23.1443290	16.33	B
033	4104470897830990464	278.5822511	-14.3406907	18.2360939	-2.7875174	16.37	A
034	5934751007588607616	244.2287289	-51.5584142	331.9908631	-0.6708695	16.39	A
035	4040806872563108736	267.9705341	-34.9748899	355.4993650	-4.2436140	16.46	A
036	1899263645288575232	333.5701007	33.1238321	88.7843066	-19.1293885	16.47	A
037	4043988927861984256	269.7853139	-31.5969500	359.1920881	-3.8662686	16.48	B
038	4056260504334777856	269.6764775	-29.8055925	0.7036549	-2.8962750	16.51	A
039	4043160166667499392	268.7876558	-33.6170544	357.0164674	-4.1432569	16.51	A+B
040	6064734619321769856	207.0171663	-55.3840033	310.9724261	6.6011920	16.52	A
041	4039570020686594304	272.3027922	-33.7608736	358.3209432	-6.7678286	16.56	A
042	4119903643141485824	266.0036138	-19.4118124	7.9532570	5.2698599	16.57	A
043	4041998223399082752	270.1778302	-35.1540559	356.2447677	-5.9003667	16.59	A
044	5946723452194568704	264.7253653	-50.3535242	340.9413001	-10.0417012	16.60	A
045	4045413207825559808	274.3978285	-33.5364601	359.3393230	-8.2074141	16.60	A
046	4064632323134994816	272.8062077	-26.1704776	5.2316184	-3.5359947	16.61	B
047	4055692507632670720	268.0851347	-31.2949870	358.7251839	-2.4599644	16.62	A
048	4053054431284531968	274.4009350	-25.8347569	6.2088590	-4.6391281	16.65	B
049	4049116805296535296	271.8379282	-31.2615423	0.3424126	-5.2319770	16.66	B
050	4063140771207991168	271.0991224	-27.3203639	3.4851742	-2.7580522	16.67	A
051	443788525336160512	57.0194916	52.7031377	147.9094846	-1.3833894	16.68	A
052	5960669348421847040	265.1301564	-40.6199623	349.4853810	-5.2296012	16.70	A
053	4050164747272227584	270.5812067	-30.3334375	0.6310845	-3.8377637	16.70	A+B
054	4077869107439976320	278.4208477	-23.2662270	10.1877968	-6.7097222	16.73	A
055	4064540513876708096	273.1534553	-26.7648570	4.8568517	-4.0928488	16.75	B
056	4065624361840345088	274.1892381	-23.3639956	8.3030297	-3.3059357	16.76	B
057	4254983555662524288	283.5813926	-4.6656679	29.1048953	-2.7665401	16.79	A
058	4105328207729395584	280.7047581	-13.5224417	19.9060564	-4.2487467	16.80	A
059	4041267941519396352	264.8862278	-35.1859206	354.0074049	-2.1951870	16.85	A
060	5962405713502000768	265.4393819	-37.0974025	352.6188565	-3.5844998	16.87	A
061	4063286589604553600	271.6101851	-26.6629815	4.2820978	-2.8352249	16.89	A
062	5933611054559826944	247.0982980	-53.1454425	332.1007425	-3.0324750	16.91	A
063	5853767990462652032	213.3033358	-63.5950879	311.8743962	-2.1521389	16.94	A
064	4043698789930892160	270.1587362	-32.2749798	358.7574490	-4.4763817	16.95	B
065	5900412881430948608	226.8217997	-51.5178025	323.3866456	5.8769005	16.98	A

Continued on next page

Table D.1 – continued from previous page

GaiaDR3- ULENS-	Gaia DR3 sourceid	RA _{J2000} [deg]	Dec _{J2000} [deg]	Gal.long. [deg]	Gal.lat. [deg]	Baseline G [mag]	Method
066	4048971261782646528	272.9183590	-31.3252741	0.7277628	-6.0742305	17.00	A+B
067	4042928139682133120	270.2881994	-32.5577055	358.5641559	-4.7103806	17.02	A
068	4053988127168351104	267.0739349	-32.8775550	356.9254031	-2.5331136	17.04	B
069	4043375503532180608	269.0711792	-32.4500107	358.1485840	-3.7652406	17.08	A
070	4091460990925014528	275.5313927	-20.1550981	11.7261426	-2.8974067	17.11	B
071	4090523111881884416	273.9130130	-22.3512268	9.0753924	-2.6019945	17.12	A
072	6057091226831797632	193.5817284	-59.1361017	303.3032122	3.7335642	17.13	A
073	4050046339277832832	272.4689862	-30.0405762	1.6797474	-5.1244076	17.14	A
074	5958979330397499392	264.1271363	-42.2729117	347.6769302	-5.4647202	17.14	A+B
075	5946702939434812800	265.5939850	-49.2145748	342.2266449	-9.9450824	17.16	A
076	4041606110282426624	268.4350280	-34.2213035	356.3451998	-4.1934739	17.19	B
077	4063274151469596928	271.7184311	-26.7337580	4.2671704	-2.9541322	17.19	B
078	4042619211263272960	270.9847730	-33.6993888	357.8479186	-5.7757472	17.20	B
079	4050127359632060672	271.8932501	-29.7381780	1.7060521	-4.5413865	17.23	A
080	4043611005164862336	268.5469471	-32.0885254	358.2389748	-3.2004290	17.25	A
081	4268189072623902976	288.5624318	2.9221359	38.1424521	-3.7313608	17.27	B
082	5989557607714349952	236.4613593	-43.2927142	333.4771983	8.9988355	17.29	A
083	4062324383827132928	269.6868712	-29.4273326	1.0367233	-2.7160153	17.30	A
084	6028177846244738944	255.9928266	-31.8704702	352.5246321	5.7855694	17.30	A
085	4052203860288017024	273.6769567	-27.9709295	4.0120583	-5.0734779	17.31	B
086	4118621539469673600	267.0133369	-21.4765031	6.6695749	3.3937819	17.32	B
087	4041534646190035456	267.4376260	-34.6244616	355.5788166	-3.6886289	17.37	A+B
088	4043504794840743040	268.1614033	-32.4895684	357.7274280	-3.1218347	17.37	A
089	4063987738711159680	270.4467027	-26.5331095	3.8853809	-1.8646211	17.38	A
090	4050237070478829696	270.0699656	-30.0015261	0.7025721	-3.2896434	17.39	B
091	4065785955602043264	272.0506217	-24.9464191	5.9772280	-2.3491989	17.39	A
092	4050901140883623296	272.9654838	-28.0545855	3.6396437	-4.5598471	17.40	B
093	5971477302907164032	253.7852905	-36.7690218	347.5207022	4.2147304	17.40	B
094	4053510694262196224	264.9520692	-33.8109647	355.2016788	-1.5105953	17.41	B
095	6028136786357495936	256.2886509	-31.8475311	352.6949212	5.5986369	17.42	A+B
096	1829267601203551488	305.3910139	22.1809621	63.1316255	-8.2590631	17.42	A
097	4068509377297713408	267.5594056	-23.6716987	5.0426374	1.8343494	17.42	B
098	4053409539185281536	265.2059834	-34.4377579	354.7814738	-2.0211318	17.48	B
099	5940987678007330816	250.5037981	-48.4425257	337.0261825	-1.4466471	17.49	A
100	4064609130464186496	272.7319736	-26.4511682	4.9527891	-3.6119659	17.50	A
101	4090456861958694784	274.5941539	-22.5706540	9.1798581	-3.2603976	17.55	A+B
102	5989806337862480256	243.9410728	-47.8559074	334.4268182	2.1240104	17.56	B
103	5969060713789360000	249.8322853	-40.8216865	342.4247810	3.9565907	17.56	B
104	4052245775095993088	274.2059498	-27.5994952	4.5620342	-5.3122062	17.56	B
105	4046296562307158784	274.2544336	-31.3835109	1.2124290	-7.1102658	17.56	B
106	5857951284237224576	200.4698542	-65.7444224	306.0551224	-3.0574410	17.59	A
107	6062116819613165952	200.4157781	-58.4573281	306.8870844	4.1821170	17.59	A
108	4040599133555482496	267.7088983	-35.9483837	354.5493178	-4.5531650	17.59	B
109	4063547483074697600	269.3491914	-27.3357397	2.7020446	-1.4146956	17.59	B
110	4059259353363569792	259.5895591	-29.8185933	356.0126907	4.4914631	17.61	A
111	4254940846504352640	283.2161231	-5.0419195	28.6038404	-2.6131505	17.63	A+B
112	5958965925733552384	262.9667349	-41.8291805	347.5873305	-4.4996535	17.66	A
113	4056324516377709184	269.0577079	-29.6127381	0.6021889	-2.3343562	17.67	A
114	4061145771721121792	262.8249712	-28.2275742	358.9201369	3.0363208	17.67	B
115	4059548250037907200	261.7620984	-29.0173858	357.7451697	3.3798476	17.71	B
116	4052262473792354432	274.8619111	-27.7150372	4.7313128	-5.8801326	17.72	A+B
117	1819571454860230400	298.4312248	15.3917600	53.8093713	-6.2759832	17.73	A
118	3355845866073702144	99.4166892	13.9551113	198.9501232	3.3306324	17.73	A+B
119	4037380691305871616	270.5039509	-36.5533798	355.1430158	-6.8108670	17.73	A
120	6030183600333074816	255.8594974	-28.5190841	355.1526169	7.8921071	17.75	A
121	4053893225594238720	265.3546739	-33.5246112	355.6222160	-1.6430896	17.75	B
122	5254312773454650880	158.7228148	-60.8680131	287.0649132	-2.2744724	17.79	A+B
123	5960494487427767040	261.7741444	-39.0160049	349.4407582	-2.1942944	17.82	A
124	4068670073424544384	267.3609727	-23.3558996	5.2205846	2.1524846	17.84	B
125	4055674881038332928	268.2522962	-31.4792946	358.6386626	-2.6764402	17.85	A
126	5864390372320262144	207.5090789	-63.4576958	309.4227326	-1.3268294	17.85	B
127	4064792821720384640	272.3866551	-26.2616693	4.9705014	-3.2495582	17.86	B
128	4043503351765043072	268.1198509	-32.5218773	357.6817483	-3.1080005	17.86	B
129	4093948842138626688	273.9036943	-20.9755081	10.2826516	-1.9405510	17.87	A
130	4065149544601352320	274.0410626	-25.1339538	6.6757581	-4.0227630	17.89	A+B
131	4063574219313975296	269.4434323	-27.1835496	2.8757834	-1.4110711	17.92	B

Continued on next page

Table D.1 – continued from previous page

GaiaDR3- ULENS-	<i>Gaia</i> DR3 sourceid	RA _{J2000} [deg]	Dec _{J2000} [deg]	Gal.long. [deg]	Gal.lat. [deg]	Baseline G [mag]	Method
132	4041815777515891456	266.7597584	-33.9288129	355.8883587	-2.8506721	17.94	A
133	4126633508902613504	252.6945648	-21.7779794	358.8621809	14.2478890	17.95	A
134	5962740239926319360	264.6305993	-36.1399213	353.0883921	-2.5270011	17.95	B
135	5909419320449816832	267.8942932	-63.7038382	329.6563000	-17.8774726	17.97	A
136	6661635838220317952	288.7314765	-47.9782019	349.5217382	-23.5592334	17.99	A
137	3012224323198211968	85.6878701	-9.3450754	213.6417900	-19.4698544	18.00	A
138	5836132614159541504	241.2056505	-56.7787973	327.1387648	-3.2897542	18.01	B
139	4058941289651705600	259.8037421	-30.9097048	355.2212356	3.7159046	18.01	A
140	5982859447285974528	237.5862424	-49.4631589	330.2113073	3.6935315	18.01	B
141	5928438230256168832	249.6186558	-57.0170251	330.2195255	-6.7138346	18.01	A
142	4110263189512077696	263.5394616	-24.8825167	2.0827199	4.3158868	18.03	A
143	6028476707251295488	255.1669862	-30.9980304	352.7939735	6.8745986	18.03	B
144	4116850741634492928	264.2705825	-22.1296842	4.7761471	5.2232028	18.03	B
145	4041835804931255808	266.3728811	-33.7500823	355.8746238	-2.4832268	18.04	B
146	4041954689781627520	267.3630208	-33.2712462	356.7117897	-2.9431717	18.06	A+B
147	4116613423221895552	264.0265519	-23.4467857	3.5371400	4.7115858	18.06	B
148	4058823431364942464	262.4470215	-29.2527327	357.8798390	2.7511817	18.07	B
149	4061084473952136832	265.4468053	-26.3589413	1.7501594	2.0737903	18.07	B
150	4146729184148567936	271.6896845	-15.2721802	14.2701216	2.6485409	18.07	A
151	4052759251109283584	275.4833650	-26.6285173	5.9567735	-5.8678536	18.10	A+B
152	5851044534497774976	208.9291129	-66.8117661	309.2106271	-4.7268194	18.11	A
153	2214532279378994816	357.6745127	69.9044944	117.7219614	7.6495224	18.11	A
154	4043049837656829696	271.1497776	-32.1075149	359.3147408	-5.1268045	18.12	B
155	4042922882640668544	270.3789088	-32.6859422	358.4895173	-4.8397995	18.13	A+B
156	4043772908261758336	269.6591664	-31.8952451	358.8790997	-3.9208361	18.13	B
157	4111395239809753856	262.1870809	-23.5200710	2.5592456	6.0914192	18.14	A
158	6733269879761239168	277.6758776	-37.0713155	357.3095656	-12.1642177	18.14	B
159	4066359454004922368	273.4280538	-23.5114232	7.8410908	-2.7612510	18.14	A+B
160	59804695213242165120	259.2930274	-31.2017926	354.7299380	3.9067554	18.15	A
161	6054706489138553728	188.7735491	-62.0918408	301.0205901	0.7192392	18.16	A
162	4065541653676268544	274.3487692	-23.9847727	7.8237512	-3.7276799	18.17	B
163	4042333814993557888	268.9132839	-34.5088596	356.2939688	-4.6791999	18.17	A
164	4178925766518902272	270.7344851	-1.5572534	25.9361418	10.0482157	18.22	A
165	4064067242840028928	269.8398302	-26.1586438	3.9410134	-1.2066784	18.24	B
166	5972707141027232896	258.9272995	-38.7666709	348.3848290	-0.2303259	18.24	A
167	4041152424074020352	265.3277727	-35.9513341	353.5476212	-2.9050249	18.24	A+B
168	5933521890952818944	247.3385750	-53.7472633	331.7628196	-3.5509832	18.24	B
169	4058485061049611264	264.1867294	-30.1761843	357.9266938	0.9810429	18.25	B
170	5977863129000915712	254.9885737	-35.1240486	349.4207187	4.4703491	18.25	A
171	4061956940776506752	265.0451994	-25.5617241	2.2366989	2.8015561	18.26	B
172	2046379503690071296	292.6789618	33.5108166	67.0297400	7.1918760	18.27	A
173	4052251547519009152	274.0496310	-27.4513041	4.6282303	-5.1202905	18.27	B
174	2073996517052513536	300.4303511	39.3734212	75.2493890	4.6788516	18.28	A
175	4059051309459806208	261.1494453	-30.1324210	356.5204941	3.2001105	18.29	B
176	4040243987040723712	266.6236609	-36.4556439	353.6629615	-4.0602281	18.29	B
177	5984758097700788992	241.2712500	-47.6031209	333.2807177	3.5304936	18.30	B
178	4090568050092602112	274.8290923	-22.1125811	9.6871182	-3.2366446	18.32	B
179	5969213344108854912	251.0201117	-39.8622421	343.7460714	3.9063263	18.34	A+B
180	5870956376488659200	207.6610129	-58.1113287	310.7058958	3.8639822	18.34	A
181	4069391146859040640	269.3111481	-23.1953382	6.2680048	0.6900547	18.37	A
182	5962745015930138112	264.4097531	-36.0880763	353.0369310	-2.3484668	18.37	B
183	4052042610131850624	277.3197534	-26.3611762	6.9502111	-7.2089360	18.37	A
184	4096791702503683200	278.1534633	-16.8257533	15.8346957	-3.5602710	18.37	A+B
185	4051359950839402368	274.4981001	-28.6545384	3.7449944	-6.0322559	18.39	A
186	4053952118170529536	266.4911297	-33.1603262	356.4302469	-2.2610615	18.40	B
187	4107328936697119232	259.2941796	-29.3325566	356.2646229	4.9805318	18.41	B
188	5864320239699873280	206.1492147	-64.5226530	308.6110530	-2.2386540	18.41	A
189	4067943919094119936	265.9940280	-25.0986050	3.0826089	2.3159390	18.42	B
190	5962559885658176128	263.2992979	-37.3678897	351.4779578	-2.2890714	18.45	A+B
191	4066190335405241216	272.9309166	-24.4845947	6.7679335	-2.8275151	18.45	A+B
192	4053892503992268288	265.2309628	-33.5649026	355.5334697	-1.5768712	18.46	B
193	4058603361633657088	262.4185974	-30.3115913	356.9814792	2.1888248	18.46	A+B
194	5256944518951207296	146.7764247	-60.8177445	282.2670572	-5.5730030	18.48	A
195	4095830312689418368	271.9424380	-18.0616657	11.9484674	1.0814379	18.48	B
196	4058430321600567552	262.8396996	-30.4251333	357.0862580	1.8228593	18.49	B
197	4511290951726598656	281.4882183	16.9668436	47.5434923	8.8260696	18.49	A

Continued on next page

Table D.1 – continued from previous page

GaiaDR3- ULENS-	Gaia DR3 sourceid	RA _{J2000} [deg]	Dec _{J2000} [deg]	Gal.long. [deg]	Gal.lat. [deg]	Baseline G [mag]	Method
198	4060933948282842368	264.4758127	-27.2098539	0.5680597	2.3568463	18.50	B
199	4505592457837046144	280.2889447	12.9315238	43.3624144	8.1025887	18.50	A
200	4042842648359086976	270.8783948	-32.9919765	358.4265239	-5.3553957	18.51	A+B
201	5861169627804660096	186.6641376	-65.2182060	300.3368129	-2.4713988	18.52	A+B
202	4077868965615513728	278.4587811	-23.2755943	10.1951268	-6.7450647	18.53	A
203	4053910130560072704	265.7712325	-33.3661346	355.9401137	-1.8551335	18.53	B
204	5877397384329104896	221.5741612	-61.8966204	316.0204839	-1.9793106	18.54	A+B
205	5977665977162203136	255.4183781	-35.2093177	349.5689039	4.1403689	18.55	A
206	4053778184815517952	264.5381698	-33.2013488	355.5335544	-0.8936310	18.55	B
207	5941348657100589824	248.7013705	-47.0729817	337.2362231	0.3697771	18.56	B
208	4063951867199966336	270.2247985	-26.8641371	3.4994252	-1.8559324	18.57	A
209	4064181184057707136	270.2787371	-25.7035632	4.5321502	-1.3234119	18.57	A
210	4058783097358064640	263.1718155	-29.3457136	358.1483266	2.1713445	18.58	B
211	5865028909305170176	202.9240268	-63.6247581	307.3854205	-1.1016564	18.58	A
212	4053432770693996416	265.6344551	-34.1037121	355.2523331	-2.1458114	18.59	B
213	4068873139592389376	267.4793217	-23.0105532	5.5731132	2.2361845	18.61	A
214	4063323530616960768	270.9486112	-26.6014298	4.0468811	-2.2890517	18.61	B
215	4065065255833603968	274.2337533	-25.7811786	6.1854205	-4.4810869	18.63	B
216	4116567308158603392	265.0202866	-22.8762171	4.5087188	4.2403523	18.63	B
217	4318866731734245504	295.5895723	16.3122565	53.2380609	-3.4483504	18.63	A
218	5870978096164685952	208.3506873	-57.8367292	311.1265654	4.0457624	18.64	A
219	4059802172898190976	260.3688199	-28.7364750	357.2933063	4.5478290	18.65	B
220	4096124500776996352	275.3708866	-18.6687694	12.9693965	-2.0671452	18.65	A
221	4042284508764889600	269.0137070	-34.6179441	356.2404416	-4.8052667	18.66	B
222	5884001227334516992	237.8343316	-56.5594625	325.8686561	-1.9225723	18.67	A
223	5940488259212239488	248.8052843	-49.5274975	335.4739259	-1.3402478	18.67	B
224	5965732938772861056	258.6423019	-42.2448818	345.4308899	-2.0805728	18.68	A
225	4041307975063716608	265.7005799	-35.1805268	354.3637083	-2.7576021	18.68	B
226	4061840461210116096	265.2607658	-26.2210375	1.7792836	2.2882464	18.69	B
227	4058004814930630912	262.3591087	-30.9817501	356.3937766	1.8620678	18.70	B
228	4100268594454909184	280.3173315	-16.0416501	17.4812714	-5.0524157	18.72	A
229	5970981388806648960	251.5222616	-38.5162735	345.0255266	4.4849943	18.72	A+B
230	4050871488475400576	272.6729789	-28.2520475	3.3422057	-4.4272717	18.73	B
231	6028410053760056576	255.3683853	-31.3316812	352.6326028	6.5349870	18.73	B
232	4096895979980830592	276.2916643	-17.1857921	14.6910688	-2.1478918	18.75	B
233	4041902669088769280	267.4801630	-33.4418828	356.6151461	-3.1145675	18.76	B
234	4067161612158838400	266.2195393	-25.5506645	2.8033588	1.9060202	18.76	A
235	5861647125082723200	193.4373693	-65.2628395	303.1739466	-2.3921771	18.77	B
236	4068464640811687808	266.9737027	-24.2389535	4.2804816	2.0017950	18.78	B
237	5980759826773028608	258.7924340	-30.3354372	355.1903571	4.7581095	18.78	B
238	6029527672875998720	254.3123343	-29.8863200	353.2277616	8.1370678	18.78	A
239	4067933920317815808	265.8492725	-25.3116082	2.8323558	2.3160490	18.79	A+B
240	4060352787652332544	263.1659130	-28.7975986	358.6055622	2.4742242	18.79	A
241	4043141200181979392	268.5875724	-33.5900499	356.9560801	-3.9855480	18.80	B
242	4049378115441315584	273.8580908	-30.7063871	1.6577039	-6.4951911	18.80	B
243	4068349462749897088	266.2994753	-23.9230249	4.2316761	2.6919627	18.81	B
244	4058980940754769792	260.1012261	-30.4782961	355.7225681	3.7517117	18.81	A
245	6057162729441951360	193.4091801	-58.7124212	303.2181457	4.1581056	18.82	A
246	4320634776479693696	288.3573682	15.5360259	49.2335302	2.2912531	18.83	A
247	5962474540419479040	264.8557139	-36.7322801	352.6825964	-2.9954043	18.83	A
248	4043628764929570688	268.3669667	-31.8911006	358.3324924	-2.9690029	18.83	B
249	4311179908525129088	282.6843949	9.1368055	40.9996588	4.3065008	18.85	A
250	5982502415238669184	238.6085150	-50.6298201	329.9810034	2.3747915	18.86	A+B
251	5961927460317472512	262.1180142	-39.2356138	349.4059653	-2.5380687	18.87	A
252	4055539469311609856	267.8331699	-32.0415212	357.9726311	-2.6551366	18.87	B
253	4060412023879926144	263.7449633	-28.1118721	359.4585551	2.4183364	18.88	B
254	4062565073796700288	269.6173841	-28.8609334	1.4982126	-2.3814400	18.90	A
255	4145925372472941568	271.9126788	-15.7912663	13.9203002	2.2087043	18.91	B
256	5931393098987729024	246.2183097	-56.2729232	329.4902619	-4.8372469	18.91	A
257	3388787058343659648	78.1420400	13.4505753	188.9801077	-14.8251729	18.92	A
258	4050797615070566016	271.7191162	-28.6009556	2.6311834	-3.8593846	18.92	B
259	5599913394301352832	116.0932117	-28.4434223	243.9996825	-2.1797752	18.94	A+B
260	4252127887751777536	283.1794554	-7.3671497	26.5116769	-3.6349108	18.94	A
261	4107297703717778688	258.8323075	-29.6422735	355.7779904	5.1308321	18.95	A+B
262	4053379891096922496	264.3814687	-34.2998834	354.5357269	-1.3716350	18.97	B
263	4167774244713700864	262.4921958	-8.1659576	15.9435442	13.9951464	18.97	A

Continued on next page

Table D.1 – continued from previous page

GaiaDR3- ULENS-	<i>Gaia</i> DR3 sourceid	RA _{J2000} [deg]	Dec _{J2000} [deg]	Gal.long. [deg]	Gal.lat. [deg]	Baseline G [mag]	Method
264	6033868957082637824	252.4820955	-27.3937210	354.2065846	10.9407916	18.98	A
265	4063248759576423936	271.5532851	-26.8501954	4.0935600	-2.8818337	18.99	B
266	4100893013996898688	283.0916163	-15.7178256	18.9702360	-7.2960920	19.01	B
267	5858050858769509888	201.1836388	-65.1703815	306.4206645	-2.5244209	19.06	B
268	4060325815241951104	264.1173268	-28.6325062	359.1962827	1.8618181	19.08	B
269	4041281792784924928	265.6908267	-35.5418934	354.0514810	-2.9403699	19.08	B
270	4060231733966232704	264.4790652	-28.5588935	359.4288328	1.6331970	19.09	B
271	5937557472277641088	251.7296056	-50.2151296	336.2042344	-3.2089269	19.09	B
272	4058601093790902528	262.3608192	-30.3921088	356.8867461	2.1860490	19.10	B
273	4060009705621629696	264.3877009	-29.6482630	358.4657249	1.1173850	19.10	B
274	4041943836257278464	266.8802288	-33.2807021	356.4958512	-2.6018684	19.11	B
275	5964077937551918720	254.8193304	-45.0878700	341.4955974	-1.5782302	19.11	B
276	5874827413327237888	224.5879126	-61.5869750	317.4355984	-2.3421590	19.16	B
277	5944591670951444224	247.5192868	-42.9198069	339.7081212	3.8115889	19.16	B
278	4040104834334974336	265.8576492	-37.0968957	352.7943555	-3.8684538	19.17	B
279	5953319864813459200	260.0530609	-43.9004978	344.6707385	-3.8768375	19.20	B
280	4041972281959897216	267.1848454	-33.1022523	356.7804102	-2.7284708	19.20	B
281	4041682221271752576	267.7460167	-33.9717257	356.2716334	-3.5750520	19.21	B
282	5970276223900786560	255.8049039	-38.6010649	347.0664085	1.8263375	19.22	B
283	4067117086266567680	266.1584137	-25.9203596	2.4590897	1.7600529	19.22	B
284	4061109904516035840	265.5054389	-26.2074578	1.9067124	2.1089310	19.22	B
285	5962697054058763776	263.9737431	-36.6927566	352.3377466	-2.3767062	19.22	B
286	4061008783736781696	265.7825648	-26.7868344	1.5441519	1.5932994	19.23	B
287	4041546122348486912	266.9522307	-34.5963319	355.3977891	-3.3312211	19.25	B
288	4061793388415544064	264.4527617	-26.4140345	1.2305039	2.7993500	19.26	B
289	5865115878111729408	200.7317435	-63.7748718	306.4025100	-1.1155151	19.27	B
290	4064049685012894080	270.0333401	-26.3194252	3.8877792	-1.4372100	19.28	B
291	5875465478011284608	229.1304472	-61.0728283	319.5831859	-2.9820985	19.29	B
292	6029920267243932288	256.4340696	-28.9850662	355.0792038	7.2097681	19.29	B
293	4043812795636739200	270.7573594	-31.9491642	359.2914624	-4.7590857	19.31	B
294	5861063421844974464	190.3513164	-64.9059182	301.8677851	-2.0549007	19.32	B
295	4060376530237310080	263.4426601	-28.4428715	359.0357556	2.4630811	19.33	B
296	4254536642846675200	285.1751116	-4.8791287	29.6355743	-4.2789489	19.35	B
297	5940833677625129472	249.4996873	-49.3354686	335.9197382	-1.5456783	19.37	B
298	5967486075708158464	251.5272560	-43.5605596	341.1828667	1.2109590	19.39	B
299	5254164713048184192	161.6595814	-60.7779843	288.2776961	-1.5074606	19.41	B
300	4060931336940814848	264.6497852	-27.2646238	0.6043286	2.1968058	19.43	B
301	5952994379322960384	258.6512536	-45.0777922	343.1291090	-3.7362420	19.46	B
302	5932291262591322240	245.5826680	-53.3436198	331.3248691	-2.5213563	19.49	B
303	4068560848199951360	267.4142708	-23.5781787	5.0547817	1.9964602	19.51	B
304	4041946924392819712	267.1120030	-33.4274199	356.4698201	-2.8433852	19.52	B
305	4043602754521124224	268.2791404	-32.2625389	357.9739153	-3.0926412	19.54	B
306	5875751076156980096	232.1402251	-60.2554703	321.2669883	-3.1024067	19.56	B
307	4068552120771025152	267.2345688	-23.7314823	4.8385648	2.0589500	19.56	B
308	5932671414400913024	240.7127685	-54.7195771	328.2975554	-1.5643581	19.57	B
309	4066693121448848384	272.7051515	-22.6155035	8.3090903	-1.7481540	19.57	B
310	4067940826629400832	266.2870015	-25.1348595	3.1902151	2.0707429	19.59	B
311	4060071931141906688	263.9390906	-29.4230961	358.4457957	1.5675481	19.60	B
312	4053693114402109568	264.3047624	-33.7152971	354.9951808	-1.0045140	19.60	B
313	4252208083428417024	283.4260287	-7.1046541	26.8571522	-3.7342959	19.61	B
314	4108068087628927488	260.8122441	-27.3216182	358.6878757	5.0208279	19.62	B
315	5861145095000219904	189.9136213	-64.4963691	301.6634513	-1.6536459	19.64	B
316	4055455219226699904	263.9980884	-30.4539634	357.6048868	0.9687776	19.66	B
317	4043093234064618240	271.3161066	-31.6786351	359.7601605	-5.0428975	19.66	B
318	5338268560822425472	162.2437459	-60.3139219	288.3209706	-0.9634122	19.82	B
319	4042335430079572480	269.1051390	-34.4097249	356.4592976	-4.7669692	19.83	B
320	4203879874428941568	283.8803402	-8.3215786	25.9720891	-4.6853379	19.85	B
321	4059443521610603136	261.8227707	-29.6841245	357.2191397	2.9657481	19.85	B
322	4037023521767456384	270.0894880	-37.7201964	353.9532983	-7.0863885	19.89	B
323	4118603058326233856	267.3982118	-21.2549663	7.0442273	3.1997564	19.91	B
324	4058624355438550400	262.5552701	-30.2487329	357.0990038	2.1248798	19.91	B
325	5877273865374753152	219.2400503	-62.8697034	314.6328332	-2.4202255	19.93	B
326	4041928271289275776	266.6457045	-33.6365566	356.0896677	-2.6183641	19.94	B
327	4044021466548302208	268.9452222	-31.7086935	358.7380941	-3.3018391	19.94	B
328	4043964322079279616	269.4002287	-31.7925309	358.8589454	-3.6789060	19.96	B
329	4064003819077926016	270.2593267	-26.3848730	3.9313389	-1.6455239	19.97	B

Continued on next page

Table D.1 – continued from previous page

GaiaDR3- ULENS-	Gaia DR3 sourceid	RA _{J2000} [deg]	Dec _{J2000} [deg]	Gal.long. [deg]	Gal.lat. [deg]	Baseline G [mag]	Method
330	5334183595902105088	173.2937682	-61.8896611	293.8530798	-0.4052851	19.99	B
331	4060858769126041344	264.9230327	-27.6781376	0.3831575	1.7714696	20.00	B
332	4060485828545912448	264.7081954	-27.7289294	0.2388613	1.9054826	20.03	B
333	5836614509548423680	239.6170816	-55.1229348	327.5572054	-1.4573336	20.04	B
334	5861190587320895104	186.9168262	-65.1816705	300.4389850	-2.4250434	20.07	B
335	4070219869407584768	268.1280807	-22.6482848	6.1901924	1.9068253	20.08	B
336	4092025491399809024	278.3416591	-20.0957119	12.9983287	-5.2116735	20.10	B
337	5892416408213499776	216.6411098	-57.1027661	315.6061919	3.4095751	20.10	B
338	4042509534992606592	269.9602053	-33.4604733	357.6393918	-4.9140219	20.11	B
339	5867019781264970496	213.1949603	-59.5612100	313.0766512	1.6988310	20.14	B
340	5932658533818012672	241.3674847	-54.8080765	328.5215242	-1.8812174	20.15	B
341	4037003833628097920	269.4667028	-37.9831402	353.4806264	-6.7850622	20.19	B
342	4041980395080048384	267.1631349	-32.8566449	356.9819395	-2.5865977	20.22	B
343	4043408626233506944	267.8664022	-33.1351658	357.0442820	-3.2359067	20.23	B
344	4068804248278621568	266.4129243	-23.2555527	4.8567259	2.9500097	20.25	B
345	4107306813251999360	258.4762371	-29.6098498	355.6244981	5.4019286	20.26	B
346	4070231689172730752	268.2801710	-22.4708390	6.4144999	1.8759243	20.29	B
347	5974617649856579456	263.0133009	-36.6151121	351.9848738	-1.6872397	20.33	B
348	4060408862783337344	263.6466765	-28.2434761	359.3008625	2.4201192	20.36	B
349	5978422166252280192	255.8815186	-33.5983108	351.0848963	4.8164961	20.37	B
350	5977975730251951872	256.0464056	-35.4189590	349.7144075	3.6060507	20.40	B
351	4069377716512265728	268.6305482	-23.2845096	5.8761169	1.1855468	20.43	B
352	4064071061114240128	270.0497131	-26.1174772	4.0704295	-1.3497038	20.47	B
353	4041642707503630208	267.6883747	-34.2447902	356.0117680	-3.6729389	20.49	B
354	5836498614158612992	239.8515774	-55.6005476	327.3480434	-1.9069641	20.53	B
355	5877288124678597760	219.3881478	-62.7202007	314.7544098	-2.3098646	20.59	B
356	4059256780768511616	259.5160288	-29.9342367	355.8809700	4.4775261	20.60	B
357	4054189784460154624	265.0965831	-32.7661462	356.1514651	-1.0582661	20.68	B
358	5962744333088467968	264.4586010	-36.0892730	353.0570410	-2.3824658	20.72	B
359	4041164935329120128	265.1614358	-35.9310040	353.4937286	-2.7799171	20.72	B
360	4054019738115896064	266.0015655	-32.9409610	356.4035158	-1.7965279	20.76	B
361	5932749758903448448	240.2786925	-54.1545852	328.4790714	-0.9727373	20.76	B
362	5938866067211518592	254.7067828	-48.4276958	338.8201608	-3.5826396	20.95	B
363	4067300223660786304	266.9193778	-25.0204118	3.5854498	1.6404974	20.97	B

Appendix E: Table with cross-match

Table E.1 lists *Gaia* DR3 events which have counterparts in other catalogues of microlensing events or real-time microlensing search programmes: OGLE-IV Bulge (Mróz et al. 2019), OGLE-IV Disk (Mróz et al. 2020b), OGLE-IV's Early Warning System web-pages (Udalski et al. 2015), KMT-Net (Kim et al. 2016), MOA (Abe et al. 1997b), ASAS-SN (Shappee et al. 2014) and *Gaia* Science Alerts (Hodgkin et al. 2021). Data from the table are also available in the on-line version of the article.

Table E.1. *Gaia* DR3 microlensing events cross-matched with other detections in OGLE, MOA, KMT-NET, ASAS-SN or *Gaia* Science Alerts surveys. There is 273 such events.

GaiaDR3- ULENS-	Cross-match
007	OGLE-2015-BLG-0064
008	BLG896.14.123
010	OGLE-2016-BLG-0133 KMT-2016-BLG-0485
011	BLG586.01.37855
013	OGLE-2015-BLG-1755
014	BLG513.13.37217 OGLE-2015-BLG-0056
018	BLG513.19.77649 OGLE-2016-BLG-1396 KMT-2016-BLG-0738
021	OGLE-2016-BLG-0357
023	GD2233.02.17021 ASASSN-16oe
025	BLG921.22.94
026	GD2110.04.10077
029	BLG518.22.135316 OGLE-2015-BLG-1578 MOA-2015-BLG-338
030	BLG523.06.68137 OGLE-2014-BLG-1948 MOA-2014-BLG-594
031	BLG513.25.80350 OGLE-2016-BLG-1654 MOA-2016-BLG-457 KMT-2016-BLG-0698
032	ASASSN-V J044558.57+081444.6
035	OGLE-2015-BLG-0128 MOA-2015-BLG-004
037	BLG507.19.46958 OGLE-2017-BLG-0033
039	BLG509.32.88384 OGLE-2016-BLG-1790 KMT-2016-BLG-1370
041	OGLE-2016-BLG-1571
043	OGLE-2015-BLG-0145
046	BLG522.16.33098 OGLE-2016-BLG-0385 MOA-2016-BLG-090 KMT-2016-BLG-1427
047	KMT-2015-BLG-0157
048	BLG529.14.92394 OGLE-2015-BLG-2098 MOA-2015-BLG-526
049	BLG573.31.86116 OGLE-2016-BLG-0322 MOA-2016-BLG-028 KMT-2016-BLG-2093
050	OGLE-2014-BLG-1991
053	BLG513.05.95050 OGLE-2017-BLG-0175 MOA-2017-BLG-071 KMT-2017-BLG-0595
054	MOA-2015-BLG-033
055	BLG523.31.89572 OGLE-2016-BLG-0085 KMT-2016-BLG-1422
056	BLG527.15.55557 OGLE-2015-BLG-0473 MOA-2015-BLG-082
059	OGLE-2015-BLG-1466
061	OGLE-2016-BLG-1864 KMT-2016-BLG-1559
062	GD1127.32.33414
064	BLG515.25.78 OGLE-2016-BLG-1866 MOA-2016-BLG-586 KMT-2016-BLG-1536
066	BLG526.16.27934 OGLE-2015-BLG-0862
067	OGLE-2015-BLG-0149 KMT-2016-BLG-1533
068	BLG660.18.34262 OGLE-2017-BLG-0140 KMT-2017-BLG-0872
069	MOA-2015-BLG-158 KMT-2016-BLG-1346
070	BLG572.15.1672
071	MOA-2017-BLG-051
073	OGLE-2015-BLG-1579 MOA-2015-BLG-398
074	BLG935.14.35174
076	BLG503.26.102570 OGLE-2017-BLG-0144 MOA-2017-BLG-001
077	BLG518.23.90006 OGLE-2016-BLG-0079 MOA-2016-BLG-023 KMT-2016-BLG-0260
078	BLG516.11.82635 OGLE-2014-BLG-1945
079	OGLE-2015-BLG-0729 MOA-2015-BLG-167 KMT-2015-BLG-0615
080	BLG535.18.21961 OGLE-2015-BLG-0255 MOA-2015-BLG-051 KMT-2015-BLG-0138
081	DG1068.02.19241
083	OGLE-2016-BLG-0125
085	BLG523.03.48248 OGLE-2015-BLG-0877 MOA-2015-BLG-216
086	BLG637.25.39934 OGLE-2015-BLG-0456
087	BLG503.23.135537 OGLE-2017-BLG-0143 MOA-2017-BLG-032 KMT-2017-BLG-1090
088	OGLE-2016-BLG-0293 MOA-2016-BLG-147 KMT-2016-BLG-1296
089	OGLE-2016-BLG-0985 KMT-2016-BLG-1569
090	BLG513.16.48941 OGLE-2015-BLG-2131
091	OGLE-2015-BLG-2112 MOA-2016-BLG-031 KMT-2016-BLG-0259
092	BLG524.32.133709 OGLE-2015-BLG-1479
093	BLG889.16.283
094	BLG661.12.38593 OGLE-2016-BLG-1299 KMT-2016-BLG-1101
095	BLG897.28.315
097	BLG639.30.78829 OGLE-2017-BLG-0260
098	BLG609.28.76 OGLE-2017-BLG-0207 KMT-2017-BLG-1397
099	GD1108.21.19118
101	BLG527.30.75497 OGLE-2014-BLG-1587 MOA-2014-BLG-528

Continued on next page

Table E.1 – continued from previous page

GaiaDR3- ULENS-	Cross-match
102	GD1137.01.17177
103	GD1102.30.23357
104	BLG523.08.47678 OGLE-2016-BLG-1762
105	Gaia17bej
108	BLG599.22.1393 OGLE-2015-BLG-0233
109	BLG645.04.59638 OGLE-2016-BLG-0025
110	OGLE-2016-BLG-1820
111	DG1029.23.41205
113	OGLE-2016-BLG-1260 MOA-2016-BLG-433 KMT-2016-BLG-0526
114	BLG612.10.58071 OGLE-2015-BLG-1656
115	BLG613.25.83084 OGLE-2017-BLG-0081 KMT-2017-BLG-2162
116	BLG531.21.154747 OGLE-2016-BLG-1366
118	GD1793.08.3677 ASASSN-16li
121	BLG661.19.35266 OGLE-2015-BLG-0224
122	GD1382.18.3097
124	BLG638.06.43147 OGLE-2015-BLG-0183
125	OGLE-2017-BLG-0065 MOA-2017-BLG-019 KMT-2017-BLG-1553
126	GD1262.09.28593
127	BLG518.27.142401 OGLE-2017-BLG-0060 KMT-2017-BLG-1228
128	BLG535.11.49818 OGLE-2017-BLG-0503 MOA-2017-BLG-174 KMT-2017-BLG-1116
130	BLG545.09.7367 OGLE-2016-BLG-0336 MOA-2016-BLG-092 KMT-2016-BLG-1406
131	BLG645.04.20686 MOA-2017-BLG-004
132	OGLE-2016-BLG-1641 MOA-2016-BLG-534 KMT-2016-BLG-1070
134	BLG610.13.87104 OGLE-2016-BLG-0464
138	GD1159.28.34506
139	BLG499.05.1914
140	GD1160.13.1131
142	OGLE-2015-BLG-0642
143	BLG885.27.55275
144	BLG621.18.15694 OGLE-2016-BLG-1883
145	BLG603.29.135144 OGLE-2016-BLG-1861
146	BLG502.24.72636 OGLE-2016-BLG-0407
147	BLG622.19.48941 OGLE-2016-BLG-0361
148	BLG613.12.125877 OGLE-2014-BLG-1521
149	BLG652.11.51046 OGLE-2016-BLG-0313 KMT-2016-BLG-0248
151	BLG530.17.93206 OGLE-2015-BLG-0347
154	BLG515.19.84730 OGLE-2016-BLG-0828
155	BLG515.06.136119 OGLE-2016-BLG-0266 MOA-2016-BLG-003 KMT-2016-BLG-1530
156	BLG507.10.125254 MOA-2014-BLG-526
158	Gaia16bnn
159	BLG544.21.82617 OGLE-2015-BLG-0427
162	BLG528.32.1070
165	BLG645.26.75287 OGLE-2014-BLG-1059
167	BLG610.19.30823 OGLE-2016-BLG-0356 KMT-2016-BLG-1629
168	GD1127.14.39807
169	BLG654.02.28137 OGLE-2017-BLG-0100
171	BLG652.30.94823 KMT-2017-BLG-0851
173	BLG523.09.72801 OGLE-2015-BLG-0607
175	BLG615.12.122 OGLE-2016-BLG-0689
176	BLG605.20.37253 OGLE-2016-BLG-0311
177	GD1144.30.787
178	BLG656.12.1967 MOA-2015-BLG-052
179	GD1093.07.26917
182	BLG610.15.14750 OGLE-2014-BLG-1608
184	BLG585.07.7110
185	OGLE-2016-BLG-0399
186	BLG660.12.67091 OGLE-2016-BLG-1873 KMT-2016-BLG-1051
187	BLG498.16.2520 OGLE-2017-BLG-0323
189	BLG633.07.23251 OGLE-2017-BLG-0516
190	BLG673.28.27627
191	BLG545.32.45815 OGLE-2015-BLG-0684
192	BLG661.11.40559 OGLE-2017-BLG-0242 KMT-2017-BLG-0929
193	BLG662.21.79580 OGLE-2015-BLG-1841
195	BLG769.23.732
196	BLG662.19.60408 OGLE-2015-BLG-1949
198	BLG675.25.90179 OGLE-2014-BLG-0993

Continued on next page

Table E.1 – continued from previous page

GaiaDR3- ULENS-	Cross-match
200	BLG516.29.58361 OGLE-2016-BLG-1484 MOA-2016-BLG-583 KMT-2016-BLG-1524
201	GD1304.24.3051
202	MOA-2017-BLG-002
203	BLG661.17.20507 OGLE-2015-BLG-0670 KMT-2016-BLG-1088
204	GD1219.15.2476
206	BLG661.32.332 OGLE-2016-BLG-0370
207	GD1114.11.1805
208	OGLE-2015-BLG-1419 MOA-2015-BLG-425
209	OGLE-2016-BLG-1133
210	BLG613.08.71969 OGLE-2017-BLG-0079 KMT-2017-BLG-0766
211	GD1268.32.3277
212	BLG603.25.85063 OGLE-2017-BLG-0157 KMT-2017-BLG-0924 Gaia17bdk
214	BLG646.03.17834 OGLE-2016-BLG-0027 KMT-2016-BLG-0261
215	BLG529.15.95592 OGLE-2015-BLG-1079
216	BLG625.12.100189 OGLE-2016-BLG-0365
219	BLG614.16.62771 OGLE-2016-BLG-0688
220	BLG571.25.2358
221	BLG509.06.60012
223	GD1116.12.4538
225	BLG604.25.52475 OGLE-2016-BLG-1382 KMT-2016-BLG-1599
226	BLG652.12.71950 OGLE-2016-BLG-0871 KMT-2016-BLG-0943
227	BLG662.05.6243 OGLE-2015-BLG-0211
229	GD2150.13.1140
230	BLG519.09.44226
231	BLG885.18.55350
232	BLG570.28.2627
233	BLG502.23.135466 OGLE-2016-BLG-0150 MOA-2016-BLG-019 KMT-2016-BLG-2501
235	GD1292.21.4478
236	BLG633.26.16850 OGLE-2016-BLG-0091 KMT-2016-BLG-0250
237	BLG617.05.57777 OGLE-2017-BLG-0165
239	BLG714.08.34194
240	KMT-2016-BLG-0868
241	BLG502.08.145185 OGLE-2017-BLG-0015 MOA-2017-BLG-070
242	BLG526.28.2567 OGLE-2016-BLG-0495
243	BLG632.05.19651 OGLE-2017-BLG-0355 KMT-2017-BLG-2002
244	BLG499.12.6674
248	BLG535.27.92999 OGLE-2017-BLG-0132 KMT-2017-BLG-1550
250	GD1161.09.16949
252	BLG535.22.22503 OGLE-2017-BLG-0543 KMT-2017-BLG-0140
253	BLG653.30.42787 OGLE-2015-BLG-0190
255	BLG767.14.27556
258	BLG519.06.147922 OGLE-2016-BLG-0081 KMT-2016-BLG-1479
259	GD1606.28.7724 Gaia17aqu
261	BLG617.22.38934 OGLE-2015-BLG-0455
262	BLG609.32.43624 OGLE-2016-BLG-0534
265	BLG518.15.121322 OGLE-2015-BLG-0254 MOA-2015-BLG-171
266	Gaia17bbi
267	GD1274.05.9905
268	BLG653.11.27375 KMT-2016-BLG-0852
269	BLG604.16.38216 OGLE-2015-BLG-0158
270	BLG653.18.3068 OGLE-2016-BLG-0190 KMT-2016-BLG-0892
271	GD1109.08.2085
272	BLG662.22.1326 OGLE-2016-BLG-1811 KMT-2016-BLG-0813
273	BLG654.18.70902 OGLE-2017-BLG-0085 KMT-2017-BLG-0736
274	BLG660.02.75339 OGLE-2015-BLG-0194
275	GD1082.31.26433
276	GD1213.04.5682
277	GD1111.25.22363
278	BLG605.07.15081 OGLE-2015-BLG-0667
279	Gaia17ahl
280	BLG660.08.86517 OGLE-2015-BLG-0808
281	BLG502.05.67258 OGLE-2016-BLG-1509 KMT-2016-BLG-1386
282	BLG998.08.18494
283	BLG683.07.41367
284	BLG652.11.33676 OGLE-2017-BLG-0286 KMT-2017-BLG-0956
285	BLG672.08.61265

Continued on next page

Table E.1 – continued from previous page

GaiaDR3- ULENS-	Cross-match
286	BLG675.26.43531 OGLE-2016-BLG-0041
287	BLG603.01.136791 OGLE-2014-BLG-1803 MOA-2014-BLG-565
288	BLG667.01.7909 OGLE-2016-BLG-0122 KMT-2016-BLG-0961
289	GD1273.06.52572
290	BLG646.16.38801 OGLE-2016-BLG-0059 KMT-2016-BLG-1575
291	GD1202.12.28001
292	BLG894.03.9531
293	BLG515.29.111770 OGLE-2014-BLG-1664
294	GD1297.13.4851
295	BLG653.24.13071
296	DG1041.09.1613
297	GD1116.09.42264
298	GD1096.05.24355
299	GD1369.23.25570
300	BLG675.24.114167 OGLE-2016-BLG-0428 KMT-2016-BLG-0978
301	GD1909.29.25476
302	GD1134.05.55989
303	BLG639.31.35102 OGLE-2017-BLG-0261 KMT-2017-BLG-2017
304	BLG502.25.124534 OGLE-2017-BLG-0264 KMT-2017-BLG-0879
305	BLG535.19.77280 OGLE-2015-BLG-0284 MOA-2015-BLG-104
306	GD1188.07.5777
307	BLG639.32.1758 OGLE-2014-BLG-1058
308	GD1157.19.6827
309	BLG543.16.58089 OGLE-2016-BLG-1754 Gaia17bbs
310	BLG633.05.33870 OGLE-2016-BLG-1855 KMT-2016-BLG-1215
311	BLG654.29.32704 OGLE-2017-BLG-0087 KMT-2017-BLG-0747
312	BLG661.16.9749 OGLE-2017-BLG-0213 KMT-2017-BLG-0678
313	DG1030.04.3259
314	BLG921.23.4257 KMT-2017-BLG-0653
315	GD1297.23.38557
316	BLG654.03.51419 OGLE-2015-BLG-1600
317	BLG514.01.66114 OGLE-2015-BLG-0252
318	GD1368.05.3561
319	BLG509.13.122856 OGLE-2015-BLG-0141
320	DG1031.02.9498
321	BLG615.17.48284 OGLE-2017-BLG-0113 KMT-2017-BLG-1942
322	BLG537.17.11402
323	BLG637.31.2736
324	BLG662.21.34275
325	GD1232.09.44403
326	BLG603.28.35150 KMT-2016-BLG-2061
327	BLG507.14.185211 OGLE-2017-BLG-0032 MOA-2017-BLG-021 KMT-2017-BLG-0104
328	BLG507.12.63267 OGLE-2017-BLG-0031 KMT-2017-BLG-0098
329	BLG646.15.2528 OGLE-2015-BLG-0925
330	GD1338.14.2320
331	BLG675.14.31799 OGLE-2016-BLG-1475 KMT-2016-BLG-0970
332	BLG675.07.100337 OGLE-2016-BLG-1862 KMT-2016-BLG-2291
333	GD1157.14.5178
334	GD1304.23.13626
335	BLG638.18.94340 OGLE-2016-BLG-0053
336	BLG563.14.46178
337	GD1227.05.19355
338	BLG508.01.34340 OGLE-2017-BLG-0539
339	GD1242.02.14463 Gaia16aua
340	GD1149.07.11095
341	BLG537.12.70927
342	BLG660.17.94309 OGLE-2017-BLG-0817 KMT-2017-BLG-0871
343	BLG502.29.100629 OGLE-2017-BLG-0095 MOA-2017-BLG-160 KMT-2017-BLG-1123
344	BLG632.21.71948 OGLE-2017-BLG-0563 KMT-2017-BLG-1073
345	BLG617.24.41328 OGLE-2016-BLG-0231
346	BLG642.16.64346
347	BLG672.22.32355 OGLE-2015-BLG-1558
348	BLG653.30.92569 OGLE-2015-BLG-0191
349	BLG898.13.20247
350	BLG900.29.16170
351	BLG643.23.58194 OGLE-2015-BLG-1555

Continued on next page

Table E.1 – continued from previous page

GaiaDR3- ULENS-	Cross-match
352	BLG646.25.18413 OGLE-2017-BLG-0441 KMT-2017-BLG-1371
353	BLG503.30.103160 OGLE-2017-BLG-0145 MOA-2017-BLG-095 KMT-2017-BLG-2618
354	GD1158.31.47588
355	GD1232.17.23871
356	BLG617.09.66418
357	BLG679.04.38335 KMT-2017-BLG-0867
358	BLG610.14.97071 OGLE-2016-BLG-1727
359	BLG610.20.3895 OGLE-2016-BLG-1408 KMT-2016-BLG-1630
360	BLG660.15.22580 OGLE-2017-BLG-0307 KMT-2017-BLG-0856
361	GD1156.03.7788
362	GD1092.18.44649
363	BLG633.01.52040 OGLE-2017-BLG-0116 KMT-2017-BLG-1029

Notes. OGLE survey detections come either from the EWS (OGLE-year-field-nnnn) or catalogues published in [Mróz et al. \(2019\)](#) and [Mróz et al. \(2020b\)](#) (BLGnnn.nn.nnnn or GDnnnn.nn.nnnnn).